University of Reading

Intraseasonal variability of air-sea fluxes over the Bay of Bengal during the southwest monsoon

Article

Published Version

Creative Commons: Attribution 4.0 (CC-BY)

Open Access

It is advisable to refer to the publisher's version if you intend to cite from the work. See Guidance on citing.

To link to this article DOI: http://dx.doi.org/10.1175/JCLI-D-17-0652.1

Publisher: American Meteorological Society

www.reading.ac.uk/centaur

CentAUR

Central Archive at the University of Reading

Reading's research outputs online

ᓂ Intraseasonal Variability of Air–Sea Fluxes over the Bay of Bengal during the Southwest Monsoon⟋

Alejandra Sanchez-Franks and Elizabeth C. Kent

National Oceanography Centre, Southampton, United Kingdom

Adrian J. Matthews and Benjamin G. M. Webber

*Centre for Ocean and Atmospheric Sciences, School of Environmental Sciences,
University of East Anglia, Norwich, United Kingdom*

Simon C. Peatman

National Centre for Atmospheric Science–Climate, University of Reading, Reading, United Kingdom

P. N. Vinayachandran

Centre for Atmospheric and Oceanic Sciences, Indian Institute of Science, Bangalore, India

ABSTRACT

In the Bay of Bengal (BoB), surface heat fluxes play a key role in monsoon dynamics and prediction. The accurate representation of large-scale surface fluxes is dependent on the quality of gridded reanalysis products. Meteorological and surface flux variables from five reanalysis products are compared and evaluated against in situ data from the Research Moored Array for African–Asian–Australian Monsoon Analysis and Prediction (RAMA) in the BoB. The reanalysis products: ERA-Interim (ERA-I), TropFlux, MERRA-2, JRA-55, and CFSR are assessed for their characterization of air–sea fluxes during the southwest monsoon season [June–September (JJAS)]. ERA-I captured radiative fluxes best while TropFlux captured turbulent and net heat fluxes Q_{net} best, and both products outperformed JRA-55, MERRA-2, and CFSR, showing highest correlations and smallest biases when compared to the in situ data. In all five products, the largest errors were in shortwave radiation Q_{SW} and latent heat flux Q_{LH}, with non-negligible biases up to approximately $75 \, \text{W m}^{-2}$. The Q_{SW} and Q_{LH} are the largest drivers of the observed Q_{net} variability, thus highlighting the importance of the results from the buoy comparison. There are also spatially coherent differences in the mean basinwide fields of surface flux variables from the reanalysis products, indicating that the biases at the buoy position are not localized. Biases of this magnitude have severe implications on reanalysis products' ability to capture the variability of monsoon processes. Hence, the representation of intraseasonal variability was investigated through the boreal summer intraseasonal oscillation, and we found that TropFlux and ERA-I perform best at capturing intraseasonal climate variability during the southwest monsoon season.

1. Introduction

Circulation in the Indian Ocean is governed by monsoon variability (Goswami 2012; Weller et al. 2016). In the Bay of Bengal (BoB), sea surface temperature (SST)

and heat flux are the key components in southwest (SW) monsoon behavior (Vecchi and Harrison 2002; Parampil et al. 2010; Vialard et al. 2012). The mechanism via which the surface net heat fluxes Q_{net} impact SST variability is linked to the BoB barrier layer (Duncan and Han 2009). During the summer, a combination of increased precipitation and river runoff in the northern BoB contributes to the formation of a highly stratified surface barrier layer that sits above the thermocline and below the mixed layer base (Vinayachandran et al. 2002). The summer barrier layer acts to inhibit processes such as entrainment, vertical advection, and upwelling, which result in surface Q_{net} having a greater impact on the intraseasonal SST variability (Duncan and Han 2009).

The importance of the Q_{net} as a driver of summer SST variability in the BoB (Duncan and Han 2009; Goswami 2012) is also shown in observations and ocean models, where summer intraseasonal oscillations (ISOs) of SST are forced mainly by heat flux variability, with occasional contributions from vertical mixing and entrainment at the base of the mixed layer (Schiller and Godfrey 2003; Waliser 2006; Girishkumar et al. 2017). Both models and observations indicate that the intraseasonal oscillation of the northern Indian Ocean SST impacts the large-scale atmospheric wind field, temperature, humidity, and the active–break cycle of monsoon convection (Vecchi and Harrison 2002; Waliser 2006; Yang et al. 2008). Studies suggest that fluctuations in SST, driven by surface heat fluxes (Q_{net}), can be used as an indicator or proxy for the forecast of active and break periods in the monsoon (Vecchi and Harrison 2002; Parampil et al. 2010). Consequently, the accurate measurement and representation of SST and Q_{net} are critical in understanding and predicting SW monsoon processes over the BoB (Vialard et al. 2012) and monsoon variability and dynamics (Vecchi and Harrison 2002).

Several studies have reported significant differences between flux products and in situ data in the Indian Ocean (e.g., Yu et al. 2007; McPhaden et al. 2009; Kumar et al. 2012; Goswami et al. 2014; Weller et al. 2016). McPhaden et al. (2009) found that then-current numerical weather prediction (NWP) products underestimated Q_{net} by 40–60 W m^{-2} compared with in situ estimates from a moored buoy near 0°, 80.5°E. Their results suggested that the accumulation of these deficiencies in heat flux over time could result in 2°C errors in SST. Kumar et al. (2012) compared reanalysis products with moored buoy data in the global tropical oceans to create a blended flux product, TropFlux, which is based on fields from the best-performing product: the European Centre for Medium-Range Weather Forecasts (ECMWF) ERA-Interim (ERA-I) (Dee et al. 2011). They found that older reanalyses had larger biases and rms differences than ERA-I when compared to the in situ data. Yu et al.

(2007) compared NWP, reanalysis, and blended products for annual, seasonal, and interannual time scales in the Indian Ocean and found differences between 53 and 108 W m^{-2} for daily averaged measurements. Goswami et al. (2014) showed that the coupled Climate Forecast System Reanalysis (CFSR) product does not accurately simulate monsoon intraseasonal variability. These studies highlight significant shortcomings with reanalysis fields in the Indian Ocean and suggest that the accumulated errors found in reanalysis and blended products could lead to significant deficiencies in their representation of Indian Ocean processes.

To determine whether any reanalysis product gives a robust representation of monsoon processes, particularly in the BoB, it is important to understand their individual performances in representing air–sea fluxes and related meteorological parameters, such as SST, surface wind speed V, air temperature T_a, and specific humidity q_a. The products examined in this work include the atmospheric global reanalysis products: ERA-I (Dee et al. 2011); the National Aeronautics and Space Administration (NASA) Modern-Era Retrospective Analysis for Research and Applications, version 2 (MERRA-2) (Rienecker et al. 2011); the Japan Meteorological Agency (JMA) Japanese 55-year Reanalysis (JRA-55) (Kobayashi et al. 2015); the National Centers for Environmental Prediction (NCEP) CFSR (Saha et al. 2010); and the air–sea flux product focused on the tropical oceans, TropFlux (Kumar et al. 2012). The products are assessed using in situ data from the Research Moored Array for African–Asian–Australian Monsoon Analysis and Prediction (RAMA) (McPhaden et al. 2009). The BoB is a region where monsoon processes are still not fully understood (Weller et al. 2016) and in situ data are sparse (Vinayachandran et al. 2018), making gridded reanalysis products hard to verify.

Section 2 gives a brief overview of the datasets used in this paper, including four reanalysis products, a blended product, and in situ data. The analysis and discussion of air–sea fluxes in the BoB for the SW monsoon season [June–September (JJAS)] is presented in sections 3, 4, and 5. There is a comparison of reanalysis products with in situ data from RAMA buoys in the BoB for interannual variability (section 3), an in-depth analysis of individual flux components (section 4), and an evaluation of the reanalysis products' characterization of basinwide air–sea fluxes and the associated intraseasonal variability from the boreal summer intraseasonal oscillation (section 5). A summary is given in section 6.

2. Data and methods

The characterization of air–sea fluxes in the BoB from flux products is investigated using meteorological (SST, V, T_a, and q_a) and flux parameters [shortwave radiation

TABLE 1. Summary of reanalysis, blended (marked with an asterisk), and in situ products used in this study.

Product	Input SST	Resolution	Period	Reference	Flux method
ERA-Interim	See Dee et al. (2011)	Subdaily (3 and 6 hourly), 0.75° × 0.75°	1979–present	Dee et al. (2011)	Model
TropFlux*	Bias-corrected ERA-I	Daily, 1.0° × 1.0°	1979–present	Kumar et al. (2012)	COARE3.0
JRA-55	Centennial Observation-Based Estimates (COBE) SST (Ishii et al. 2005)	Subdaily (3 and 6 hourly), 0.56° × 0.56°	1979–present	Kobayashi et al. (2015)	Model
MERRA-2	See Bosilovich et al. (2015)	Subdaily (1 hourly), 0.5° × 0.625°	1980–present	Bosilovich et al. (2015)	Model
CFSR	See Saha et al. (2011)	Subdaily (6 hourly), 0.5° × 0.5°	1979–2011 CFSv2: 2011–present	Saha et al. (2010) Saha et al. (2011)	Model
RAMA	Observed	Subdaily (1-hourly fluxes; 2-min radiation data; and 10-min surface meteorological data)	2007–present	McPhaden et al. (2009)	COARE3.0

Q_{SW}, longwave radiation Q_{LW}, sensible heat flux Q_{SH}, latent heat flux Q_{LH}, and Q_{net}] from four reanalysis products, one blended product, and in situ data from the RAMA. The surface fluxes from the reanalysis products are model fluxes; turbulent fluxes for RAMA and TropFlux are calculated from meteorological parameters following Fairall et al. (2003); and radiative fluxes are measured by RAMA and derived as described in Kumar et al. (2012) for TropFlux. In all reanalysis (and blended) datasets, T_a and q_a are provided at 2-m height above sea level, and V is provided at 10 m. The in situ buoy data measure T_a and q_a at 3 m and V at 4 m, which are adjusted to 2 and 10 m, respectively, using the COARE, version 3.0, algorithm (Fairall et al. 2003). Note, q_a is not available from ERA-I or at the RAMA sites. Instead, we use dewpoint temperature from ERA-I and relative humidity in the case of RAMA, from which we derive the vapor pressure e and thus calculate q_a, as per Bolton (1980),

$$q_a = \left[\varepsilon \frac{e}{p - e(1 - \varepsilon)} \right] \times 1000, \qquad (1)$$

where p is surface pressure, and $\varepsilon = 0.622$ is the ratio of the molecular masses of water vapor and dry air. Similarly the specific humidity at the sea surface q_s is computed from SST as per Eq. (1), where the saturation specific humidity is assumed to be at 98% saturation at the SST.

Data were obtained at the temporal resolutions described in section 2a for JJAS from 2007 to 2015 and then daily averaged, as daily resolution is adequate for resolving intraseasonal variability, which is the primary mode of variability for monsoonal processes. In the following sections, both meteorological and flux variables from the reanalysis data have been regridded to 1° × 1°, by linear interpolation, where necessary. The

data products used in this paper are briefly described here and in Table 1.

a. Reanalysis and blended products

ERA-I is a global atmospheric reanalysis product from the ECMWF (Dee et al. 2011). The data assimilation system for ERA-I uses four-dimensional variational (4D Var) analysis, with an improved hydrological cycle and quality control compared with the previous ECMWF reanalysis product, ERA-40 (Berrisford et al. 2011). The mean state variables used here are from the analysis field (step 0) at 6-hourly time intervals and the flux variables are from the forecast field (step 12) at 3-hourly time intervals. All variables are obtained on a 1° × 1° horizontal grid.

TropFlux is a blended (reanalysis based) product of air–sea fluxes and associated meteorological variables over the global tropical oceans, from 30°S to 30°N (Kumar et al. 2012, hereinafter KP12). TropFlux uses satellite cloud data from ISCCP (Zhang et al. 2004) to compute Q_{SW} and bias-adjusted ERA-I (Dee and Uppala 2009) data to compute SST, V, T_a, q_a, and Q_{LW} as

$$\Psi_{tf}(x,y,t) = a[\Psi(x,y,t) - \overline{\Psi}(x,y)] + b(x,y) + \overline{\Psi}(x,y), \qquad (2)$$

where Ψ_{tf} is the corrected ERA-I variable Ψ, and the long-term mean is $\overline{\Psi}$. The amplitude a and bias b adjustments of the TropFlux variables are based on a comparison between the reanalysis product and in situ data from the Global Tropical Moored Buoy Array (McPhaden et al. 2010). The turbulent fluxes were computed using the COARE, version 3.0 (COARE3.0), algorithm (Fairall et al. 2003) on the corrected daily averaged input variables and, since TropFlux computes

heat fluxes from daily averaged data, a gustiness correction is applied to the surface wind speed parameter to compensate for the higher-frequency (<1 day) fluctuations in wind speed, which result in underestimations in the flux variability based on results of Cronin et al. (2006). The cool skin and warm layer calculations in COARE, version 3.0, are switched off (KP12). The gustiness correction is applied to the surface wind speed parameter only for the computation of turbulent heat fluxes. The TropFlux data are served as daily means on a 1° × 1° horizontal grid. The spatially homogeneous amplitude adjustment a acts to increase the variance of all the parameters in ERA-I around their long-term values. We note that TropFlux adjusts ERA-I meteorological parameters based on measurements from the Global Tropical Moored Buoy Array, however, only data to the end of 2009 were available at the time TropFlux was produced. At this time RAMA had only recently been established: Measurements at mooring b28 started in November 2006, with moorings b26 and b27 being added a year later. The observational constraints will therefore be dominated by the longer-established moorings in the Pacific, and to a lesser extent, in the Atlantic.

JRA-55 is the second global atmospheric reanalysis product produced by the JMA (Kobayashi et al. 2015), built to improve upon JRA-25 (Onogi et al. 2007). JRA-55 has a new longwave radiation scheme, increased spatial resolution, and uses variational bias correction (VarBC) and 4D Var analysis. The data used here are on a 0.56° × 0.56° grid, using analysis fields for the mean state variables and 3-hourly averages for the flux variables.

MERRA-2 is a global atmospheric reanalysis of the satellite period produced by NASA (Bosilovich et al. 2015), and updated from the original MERRA product (Rienecker et al. 2011). MERRA-2 uses an updated atmospheric data assimilation system: the Goddard Earth Observing System Model, version 5 (GEOS-5), with a three-dimensional variational (3D Var) analysis algorithm. Important updates to MERRA-2 since the original MERRA product also include an updated observing system with more satellite observations and an aerosol analysis (Bosilovich et al. 2015). The MERRA-2 data have a spatial resolution of 0.5° latitude by 0.625° longitude on 72 levels. Here, the mean state variables are at 1-hourly, instantaneous, single-level diagnostics and the flux variables are 1-hourly, time-averaged, radiation diagnostics.

CFSR is a coupled ocean–atmosphere reanalysis product created by NCEP (Saha et al. 2010). The Climate Forecast System model that CFSR uses includes a spectral atmospheric model and the Modular Ocean Model from the Geophysical Fluid Dynamics Laboratory. The atmospheric model has a spatial resolution of 0.5° × 0.5° on 37 vertical levels, and the ocean model has a resolution of 0.5° on 40 vertical levels. CFSR was completed for the period 1979–2009 and was later extended to 2011. In 2011, CFSv2 was implemented as a continuation of CFSR (Saha et al. 2011). As CFSv2 uses the same model as CFSR, the CFSv2 product is treated as an extension of CFSR, and CFSv2 is hereafter implied in any mention of CFSR. The data were available at 6-h forecast field for mean state variables and at 6-h averaged field for flux variables.

All reanalysis products assimilate ocean observations from fixed mooring arrays, including the Global Tropical Moored Buoy Array (McPhaden et al. 2010).

b. In situ data: The RAMA

RAMA is an array of moored buoys in the Indian Ocean that provide atmospheric and oceanographic data for the study of ocean circulation, air–sea interactions, and monsoon dynamics (McPhaden et al. 2009). The types of moored buoys relevant for this study within the RAMA network are the surface and enhanced surface moorings. The enhanced surface moorings are Autonomous Temperature Line Acquisition System (ATLAS) moorings with additional sensors for pressure and longwave radiation measurements designed for measuring complete air–sea interactions and are denominated flux reference sites. In the BoB, there are two surface moorings located at 8°N, 90°E (designated b26) and 12°N, 90°E (b27), and one enhanced surface mooring at 15°N, 90°E (b28).

Meteorological variables used include SST (measured at 1 m below sea surface), V (measured at 4 m above sea surface and converted to 10-m height by the data providers), T_a (measured at 3 m above sea surface and adjusted to 2 m), and relative humidity (measured at 3 m above sea surface and adjusted to 2 m), and q_a is computed from T_a and pressure as in Eq. (1). All height adjustments use the COARE3.0 algorithm as per Fairall et al. (2003). Table 2 shows the uncertainties for the meteorological variables (SST, V, T_a, and humidity), which correspond to the Next Generation ATLAS Mooring Sensors accuracies listed on the NOAA/PMEL website (https://www.pmel.noaa.gov/gtmba/sensor-specifications). These accuracies are based on calibrations for predeployment and postrecovery. ΔT and Δq uncertainties are calculated using quadrature (Table 2).

The air–sea flux variables are computed using the COARE, version 3.0b, algorithm (Fairall et al. 2003; Cronin et al. 2006) by data providers. Net radiative fluxes, also calculated by providers, were calculated from

TABLE 2. Summary of documented (SST, V, T_a, and q_a) uncertainties (McPhaden et al. 2009) and calculated (ΔT, Δq, Q_{SH}, and Q_{LH}) uncertainties from the RAMA buoy instruments.

Measurement	Uncertainty
SST	$\pm 0.02°C$
V	$\pm 0.2\,m\,s^{-1}$
T_a	$\pm 0.2°C$
q_a	$\pm 0.2\,g\,kg^{-1}$
ΔT	$\pm 0.2°C$
Δq	$\pm 0.28\,g\,kg^{-1}$
Q_{SH}	$\pm 2.5\,W\,m^{-2}$
Q_{LH}	$\pm 7.3\,W\,m^{-2}$

FIG. 1. Availability of data at buoy site b28 (15°N, 90°E) for meteorological and flux parameters used in this study.

measured downwelling components following Cronin et al. (2006) such that

$$Q_{SW} = (1 - \alpha)SWR \quad \text{and} \tag{3}$$

$$Q_{LW} = \varepsilon(\beta T_s^4 - LWR), \tag{4}$$

where α is a constant albedo (0.055), SWR is the incoming downwelling radiation, ε is the emissivity (0.97), β is the Stefan–Boltzman constant ($5.67 \times 10^{-8}\,W\,m^{-2}\,K^{-4}$), T_s is the skin temperature (K), and LWR is the incoming downwelling longwave radiation. For the turbulent fluxes, biases from daily resolved wind speed in the RAMA fluxes (computed using COARE3.0) are minimized by applying a gustiness correction in the wind speeds prior to their use in the bulk flux calculations as per Cronin et al. (2006). We estimated the turbulent flux uncertainties (Table 2) from the standard deviation of differences between RAMA turbulent fluxes (calculated using hourly data input for the COARE3.0 algorithm, including cool skin and warm layer effects) and turbulent fluxes estimated from RAMA meteorological variables perturbed with the instrument uncertainties [input data were daily averaged in the COARE3.0 algorithm, and as per Cronin et al. (2006) cool skin and warm layer effects were turned off]. We note that there is a mean difference of 0.13 and 2.25 $W\,m^{-2}$ for Q_{SH} and Q_{LH}, respectively, when comparing turbulent fluxes estimated from hourly averaged data (cool skin and warm layer effects turned on) and daily averaged data (cool skin and warm layer turned off). Subsets of RAMA data can be obtained from the TAO Project Office of NOAA/PMEL, where meteorological and flux variables are available at high (up to 10 min) resolution. All meteorological and flux variables are presented in this paper averaged to give daily resolution.

The RAMA moorings in the BoB have been operational since 2007; however, issues in buoy maintenance affect data return, resulting in intermittent data coverage (McPhaden et al. 2010). Figure 1 shows the availability of parameters used in this study at b28. As b27
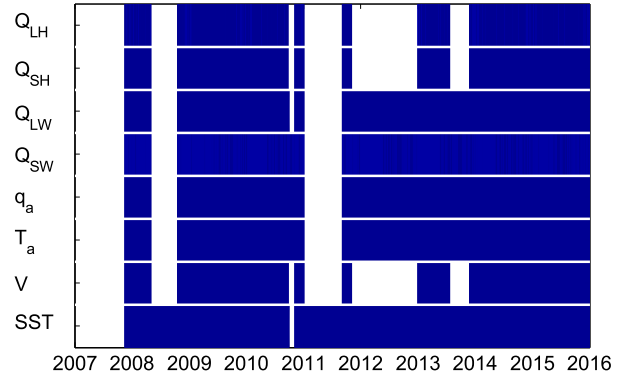
and b26 are not flux reference sites, pressure (hence q_a) and Q_{LW} are not available at these buoy locations (not shown here). The most comprehensive coverage occurs at site b28, with almost complete data return in SST. Noticeable gaps for the remaining variables occur mostly during 2007, 2008, 2011, 2012, and (for V and turbulent fluxes only) 2013. Because of the data limitation at sites b27 and b26, the following time series analysis using reanalysis products and the RAMA buoys will focus only on data from site b28.

3. Evaluation of meteorological and flux variables

In this section, the five data products are evaluated against in situ data from the RAMA buoy b28 in the BoB for JJAS from 2007 to 2015. We evaluate the meteorological parameters important for calculation of turbulent fluxes: SST, V, T_a, and q_a, as well as the air–sea temperature difference ΔT, the air–sea humidity difference Δq, the turbulent fluxes Q_{SH} and Q_{LH}, the radiative fluxes Q_{SW} and Q_{LW}, and the Q_{net}. In the following section, meteorological variables are further investigated to understand their impact on the turbulent fluxes in this region and the causes for disparities in the products' ability to represent surface fluxes.

Individual daily values of the surface fluxes and associated variables for each of the products are compared to RAMA buoy b28 using four metrics. First the differences (product minus b28) and their 95% confidence intervals (calculated using a t test implemented in R using function t.test; R Core Team 2015) are presented (Fig. 2a). Second, the Pearson product moment correlation coefficients for each product with b28 and their 95% confidence intervals (calculated in R using function cor.test) are presented (Fig. 2b). Figure 2c shows the variance ratio of the parameters with their 95% confidence interval (calculated using an F test implemented
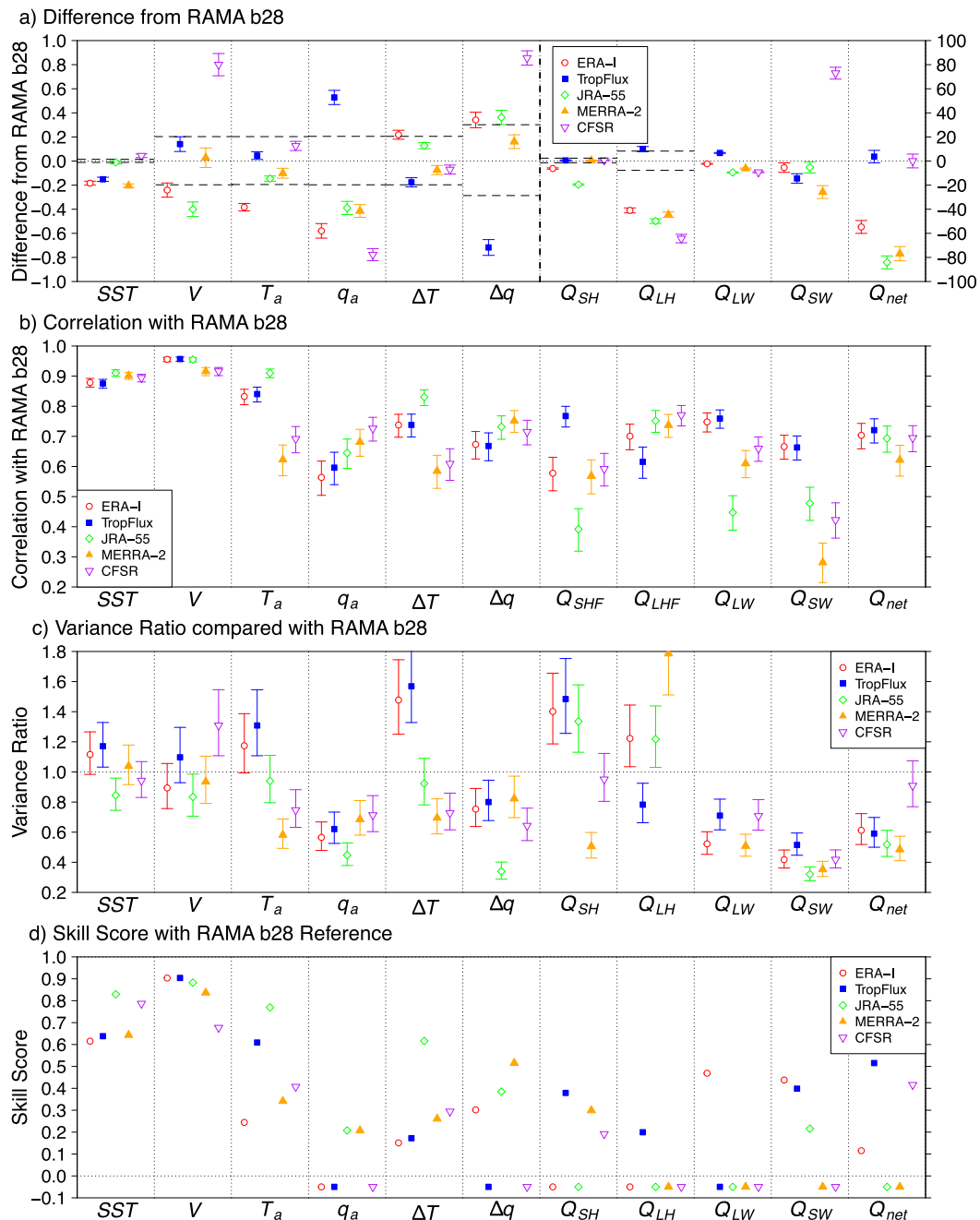
FIG. 2. (a) Difference (product minus RAMA), (b) correlation, (c) variance ratio, and (d) skill score for re-analysis products (ERA-I, TropFlux, JRA-55, MERRA-2, and CFSR) against data from RAMA buoy b28. The 95% confidence intervals are shown in the difference, correlation, and variance ratio metrics. The variables evaluated are the meteorological parameters SST (°C), V (m s^{-1}), T_a (°C), q_a (g kg^{-1}), ΔT (°C), and Δq (g kg^{-1}) and fluxes Q_{SW} (W m^{-2}), Q_{LW} (W m^{-2}), Q_{SH} (W m^{-2}), Q_{LH} (W m^{-2}), and Q_{net} (W m^{-2}), for JJAS from 2007 to 2015. Uncertainties as per Table 2 are shown in (a), indicated by the horizontal dashed lines, and a split scale to dif-ferentiate between meteorological and flux parameters.

in R using function var.test). Figure 2d combines these metrics to give skill scores for each product and variable (Wallcraft et al. 2009). Skill scores are an established way to assess the quality of numerical weather forecasts

(Murphy 1988) and are based on the correlation be-tween the product being assessed and a reference stan-dard, penalized for disagreement in mean values and variance ratio. Thus, if we denote x_i (where $i = 1, \ldots, n$)

as the observations and y_i (where $i = 1, \ldots, n$) as a data product for a sample of n, we can define the linear correlation R and skill score SS, between x_i and y_i as per Murphy (1988),

$$R = \frac{1}{n} \sum_{i=1}^{n} \frac{(x_i - \overline{x})(y_i - \overline{y})}{\sigma_x \sigma_y} \quad \text{and} \quad (5)$$

$$SS = R^2 - \left(R - \frac{\sigma_y}{\sigma_x}\right)^2 - \left(\frac{\overline{y} - \overline{x}}{\sigma_x}\right)^2, \quad (6)$$

where $\overline{x}$, $\overline{y}$ and σ_x, σ_y are the sample mean and standard deviation of x_i and y_i, respectively. Skill scores of 1 demonstrate perfect agreement between the data products and the observed data. Perfectly correlated data with a 25% underestimate of variance and a bias of magnitude of 25% of the variance would have a skill score of 0.5. Negative skill scores typically arose in our comparison resulting from substantial underestimates of variance combined with large mean differences, although there were also some low correlation values.

a. Sea surface temperature

For SST, all reanalysis products show fairly strong correlations with RAMA buoy b28 (Fig. 2b). ERA-I shows the largest offset ($-0.37°C$), followed by MERRA-2 ($-0.20°C$), both underestimating the in situ SST (Fig. 2a). Both these reanalyses use the Operational SST and Sea Ice Analysis (OSTIA) foundation SST product (Donlon et al. 2012) in the period of our analysis, so are expected to have colder SSTs than a standard near-surface estimate. MERRA-2 uses OSTIA after 2006 and ERA-I from February 2009. The reason for the difference between the SST for these products is therefore not clear; their agreement improves from 2009 but remains $0.2°C$ (not shown). JRA-55 SST agrees well with b28, with the smallest bias and highest correlation (0.90; Fig. 2b), giving the highest skill in reproducing the b28 SST (Fig. 2d), despite an underestimate of the variance (Fig. 2c). The coupled product CFSR also shows a good representation of the observed SST. We note that the CFSR SST is constrained through a relaxation coefficient at the sea surface (i.e., model SST is nudged toward observed SST), which counteracts any drift in the model related to error in the surface fluxes (Xue et al. 2011). On the other hand, JRA-55, MERRA-2, and ERA-I are atmosphere-only reanalysis products with prescribed SST fields (Table 1).

b. Surface wind speed

The parameter V shows the highest correlation (≥ 0.9) across all products with V from RAMA buoy b28. TropFlux and MERRA-2 V are closest to that from b28. ERA-I and JRA-55 underestimate and CFSR overestimates

the observed V (Fig. 2a). Variance ratios are around 1, apart from CFSR, which shows significantly greater variance in V than b28 (Fig. 2c); V shows the best skill scores across the variables with ERA-I, TropFlux, and JRA all having skill scores of about 0.9 (Fig. 2d).

c. Air temperature

The highest T_a correlations are observed with ERA-I, TropFlux, and JRA-55 (≥ 0.83) and the lowest correlation with MERRA-2 (0.62) (Fig. 2b). ERA-I has the largest offset ($-0.38°C$), the other products are within $0.1°C$ of b28 (Fig. 2a). TropFlux significantly overestimates the variance, and MERRA-2 and CFSR significantly underestimate the variance (Fig. 2c). Overall JRA-55 shows the best skill, followed by TropFlux (Fig. 2d).

d. Specific humidity

The products all struggle with reproducing the observed q_a. KP12 found that ERA-I underestimated q_a and attributed more than half of that estimate to a cold bias in T_a and the remainder to an underestimate in the relative humidity. However their adjustment to q_a for ERA-I for TropFlux results in an overestimate at b28. Skill scores are all less than 0.2, resulting from a combination of modest correlations (<0.8), large mean biases ($>0.3\,\mathrm{g\,kg^{-1}}$), and a large underestimate of the variance. Our results show a CFSR dry bias also previously observed in the Maritime Continent and western Pacific by Wang et al. (2011) and overall dry bias found in ERA-I when compared to research vessel data (Brunke et al. 2011).

e. Air–sea temperature difference

For all products except ERA-I, the skill scores for ΔT are much lower than those for either SST or T_a (Fig. 2d). JRA-55 performs best, combining a small bias (Fig. 2a) with the strongest correlation (Fig. 2b) and is the only product to make a reasonable estimate of the variance (Fig. 2c).

f. Air–sea humidity difference

The skill scores for Δq for ERA-I, JRA-55, and MERRA-2 are larger than their respective skill scores for q_a, but the best skill score is only 0.5 for MERRA-2 (Fig. 2d). Modest correlations combined with large biases for most products (Fig. 2a) and a very significant underestimate of variance (Fig. 2c) give poor skill overall.

g. Shortwave radiation

For all products apart from TropFlux, biases in Q_{SW} (and Q_{LW}) are directly linked to its radiation schemes,

spatial distribution, and aerosol properties (Dee et al. 2011). TropFlux Q_{SW} uses observed cloudiness data from ISCCP up until the end of 2007 (when it was last available) and the ISCCP mean seasonal cycle and adjusted using NOAA outgoing longwave radiation (OLR) thereafter (KP12). TropFlux and ERA-I show the highest correlations (~0.7) with the observed Q_{SW} (Fig. 2b) and the highest overall skill (Fig. 2d). All of the products underestimate Q_{SW} apart from CFSR, which overestimates by more than $70\,\mathrm{W\,m^{-2}}$. MERRA-2 and CFSR show the lowest correlations (Fig. 2b) and highest biases (Fig. 2a). Positive bias in CFSR Q_{SW} in the tropics has been previously catalogued by Wang et al. (2011) caused by an underestimate of cloudiness. MERRA-2's underestimation of Q_{SW} has been similarly linked to its cloud scheme (general difficulties capturing irradiance variability) in a study by Boilley and Wald (2015). All of the products significantly underestimate the variability of Q_{SW} (Fig. 2c).

h. Longwave radiation

The skill scores for Q_{LW} are very low, with only ERA-I achieving a positive score (Fig. 2d). All products underestimate the variance (Fig. 2c) and for all of the products other than ERA-I the biases are large relative to the variability resulting in low skill.

i. Sensible heat flux

TropFlux has the most skill due to a relatively high correlation of 0.79 and a small bias of slightly over $1\,\mathrm{W\,m^{-2}}$, but overestimates the variance. ERA-I and JRA-55 have negative skill scores due to large biases and overestimates of variance. The poor skill in JRA-55 is hard to understand as it performed best at reproducing ΔT and showed high skill for V.

j. Latent heat flux

TropFlux is the only product to have a positive skill score for Q_{LH}. This is surprising as it had relatively poor skill for Δq (Fig. 2d). TropFlux underestimates Δq but shows only a small underestimate in Q_{LH}, which may indicate that the gustiness parameter used by TropFlux in the transfer coefficients may be acting to compensate for low Δq with an enhanced wind effect in the flux calculation. MERRA-2's large overestimation of Q_{LH} can be attributed to the fact that MERRA-2 has humidity (dry) bias problems related to forecast model spinup and spindown (Kobayashi et al. 2015). The large Q_{LH} bias apparent in CFSR has been observed on a global scale (larger evaporative cooling in general) and is linked to the dry bias over the equatorial Indian Ocean (Wang et al. 2011) and the erroneously strong winds (Fig. 2a).

k. Net heat flux

TropFlux has the highest skill in reproducing Q_{net}. CFSR does better than expected, despite having negative skill scores for three of the four flux components, and ERA-I is the only other product to have a positive skill score (Fig. 2d). ERA-I, JRA-55, and MERRA-2 all have too much heat loss from the ocean. TropFlux and CFSR all show a mean net heat gain by the ocean of $30–35\,\mathrm{W\,m^{-2}}$ over JJAS of 2007–15, whereas ERA-I, JRA-55, and MERRA-2 all show a net heat loss of between -20 and $-50\,\mathrm{W\,m^{-2}}$ (not shown here). We note that biases in turbulent and radiative fluxes cancel out in the Q_{net} from CFSR and (to a smaller degree) TropFlux. However, biases (mostly in Q_{SW} and Q_{LH}) carry over considerably in the Q_{net} biases estimated from ERA-I, JRA-55, and MERRA-2. Thus the blended product, TropFlux, captures the observed Q_{net} with greater skill than the reanalysis products.

Similar results are found between the reanalysis products and in situ data at other BoB RAMA buoy locations: 12°N, 90°E (b27; Fig. S1 in the supplemental material) and 8°N, 90°E (b26; Fig. S2 in the supplemental material). Based on the four metrics presented here, SST and V perform consistently well at all three locations; T_a struggles showing lower correlations and poorer skill scores at b27 and b26 (more so than at b28) and as a result ΔT and Q_{SH} are similarly poorly represented across most products. For Q_{LH}, results are consistently poor and only TropFlux shows a skill score greater than zero. Last, Q_{SW} performs similarly between products for all three buoys, that is, ERA-I and TropFlux are able to reasonably reproduce Q_{SW} while remaining products perform poorly based on mean differences, correlations, variance ratio, and skill score.

Based on the four metrics presented here, we find that ERA-I captures radiative fluxes best, while TropFlux is better at capturing the turbulent and net heat fluxes. In general, however, Q_{SW} and Q_{LH} (and Q_{net} by association) are the variables that are the hardest to capture across all products. This is evident in the low correlations, large biases, and low skill scores. Since errors in Q_{net} can cause large errors in SST in the BoB and affect the accurate representation of monsoon processes from reanalysis products, the next section investigates the flux components in more depth.

4. Surface fluxes at RAMA flux reference site b28

SST variability in the BoB is mainly driven by surface heat fluxes (Sengupta and Ravichandan 2001). Accurate representation of meteorological variables and the associated fluxes in reanalysis products is therefore crucial for

the correct representation of monsoon-related variability. The individual components of surface heat fluxes are further investigated here.

Figure 3 shows scatterplots of the Q_{net} versus each flux component from RAMA buoy b28, ERA-I, TropFlux, JRA-55, MERRA-2, and CFSR. Individual daily means are plotted as points and contours enclose 10% and 50% of the points in each joint distribution (calculated with R function HPDregionplot in the emdbook package; Bolker 2008). Figure 3a shows the relationship between Q_{SW} and Q_{net} at b28. Q_{SW} is the main driver of Q_{net} with a strong positive correlation ($r = 0.93$). Q_{LW} is anticorrelated with Q_{net} ($r = -0.58$; Fig. 3b) as increased cloud cover reduces the heat gain by the ocean by Q_{SW} and reduces the heat loss by the ocean by Q_{LW}. Both Q_{LH} and Q_{SH} are positively correlated with Q_{net} ($r = 0.68$ and 0.63, respectively; Figs. 3c,d) but Q_{LH} is an order of magnitude larger.

ERA-I shows similar correlations to b28; the correlations for the radiative components (Q_{SW} and Q_{LW}) being slightly less correlated with Q_{net} than for b28 and the turbulent components (Q_{LH} and Q_{SH}) more correlated. The underestimate of variability in Q_{SW} and Q_{LW} by ERA-I is clear in Figs. 3e and 3f, and the overestimate of Q_{LH} and resulting bias in Q_{net} in Fig. 3g. The adjustments applied to ERA-I to produce TropFlux improve performance for the TropFlux turbulent fluxes (Figs. 3k,l) to give better alignment of the distributions in addition to reducing biases. However the radiative estimates from TropFlux are worse than ERA-I. TropFlux Q_{SW} is constructed from ISCCP until 2007 and bias-corrected ISCCP mean seasonal cycle and NOAA OLR to present; hence, TropFlux Q_{SW} biases are likely linked to the algorithm used in KP12. TropFlux Q_{SW} shows improved (i.e., higher) variability, but shifts the peak of the distribution to even lower values than ERA-I (cf. Figs. 3e and 3i). The adjustments applied to ERA-I Q_{LW} to produce TropFlux worsen its performance compared with b28 (Figs. 3f,j).

The remaining three products (JRA-55, MERRA-2, and CRSR; Figs. 3m–x) all show poor agreement with the relationships between the flux components and Q_{net}, as expected from the skill scores presented in Fig. 2. The exception is the good agreement shown for CFSR Q_{SH} (Fig. 3x), but only because of the compensating biases in CFSR Q_{net}.

Deconstructing turbulent fluxes into their meteorological components provides further insight into differences among products and helps determine if errors and biases in Q_{SH} (Q_{LH}) at the buoy location (Fig. 2a) originate from errors in the wind field or air–sea contrasts in temperature (humidity). Figures 4a–f show scatterplots of Q_{LH} versus the individual components of

Q_{LH}: Δq and V. The largest contributing factor to Q_{LH} variability across all products is V, where increases in V are linked with increases in Q_{LH} (Fig. 4d). The correlation between Δq and Q_{LH} is lower (Fig. 4a) as Δq and V are anticorrelated (Fig. 4g). This anticorrelation is well captured by ERA-I (Fig. 4h) with a slight overestimate of Δq. The TropFlux corrections result in an underestimation of Δq, but despite this the Q_{LH} agrees reasonably with b28, perhaps because of the gustiness adjustment to wind in the flux calculation.

The parameter ΔT is the strongest control on Q_{SH} (Fig. 4j) with V contributing little to the variability (Fig. 4m) of Q_{SH}. This is consistent with the finding that Q_{SH} variability is particularly sensitive to SST fluctuations (cf. Q_{LH}) in the tropical Indian Ocean at intraseasonal time scales (DeMott et al. 2014). Both ERA-I (Fig. 4k) and TropFlux (Fig. 4l) overestimate the variability in ΔT. ERA-I is biased toward unstable atmospheric conditions (ΔT positive) and TropFlux overrepresents stable conditions. The TropFlux Q_{SH} is strongly skewed compared to b28, but the representation of Q_{SH} is overall better than ERA-I (Fig. 2d). The relationship between the radiative flux components at b28 (Fig. 4s) is better captured by ERA-I (Fig. 4t) than TropFlux (Fig. 4u).

In general, Q_{net} is largely driven by Q_{SW} and Q_{LH}; Q_{LH} variability is driven by V and (to a lesser extent) Δq, and Q_{SH} variability is mostly driven by ΔT. Results here suggest errors/biases in Q_{LH} originate from both the wind field and the Δq and, as Q_{SH} shows negligible dependence on V, the biases from the observed Q_{SH} are more likely to be linked with errors in the ΔT. The parameters Q_{SW} and Q_{LH} are the variables the reanalysis and blended products have the most difficulty reproducing (section 3).

5. Air–sea fluxes across the Bay of Bengal

a. Mean fields

In this section, air–sea fluxes at all points in the BoB from the reanalysis products are compared to determine how much of the variability observed at the RAMA buoy sites is localized.

Figure 5 shows turbulent fluxes from five data products averaged over the JJAS monsoon season, from 2007 to 2015, across the BoB. The Q_{SH} values from JRA-55 and (to a lesser extent) ERA-I show higher negative (upward) flux values, indicating greater heat loss from ocean to atmosphere, than the other three products. This is consistent with biases seen in section 3 (Fig. 2a), where JRA-55 and ERA-I overestimated the observed Q_{SH}. Differences in spatial gradients between products occur near b28 (black square, Fig. 5), where TropFlux,
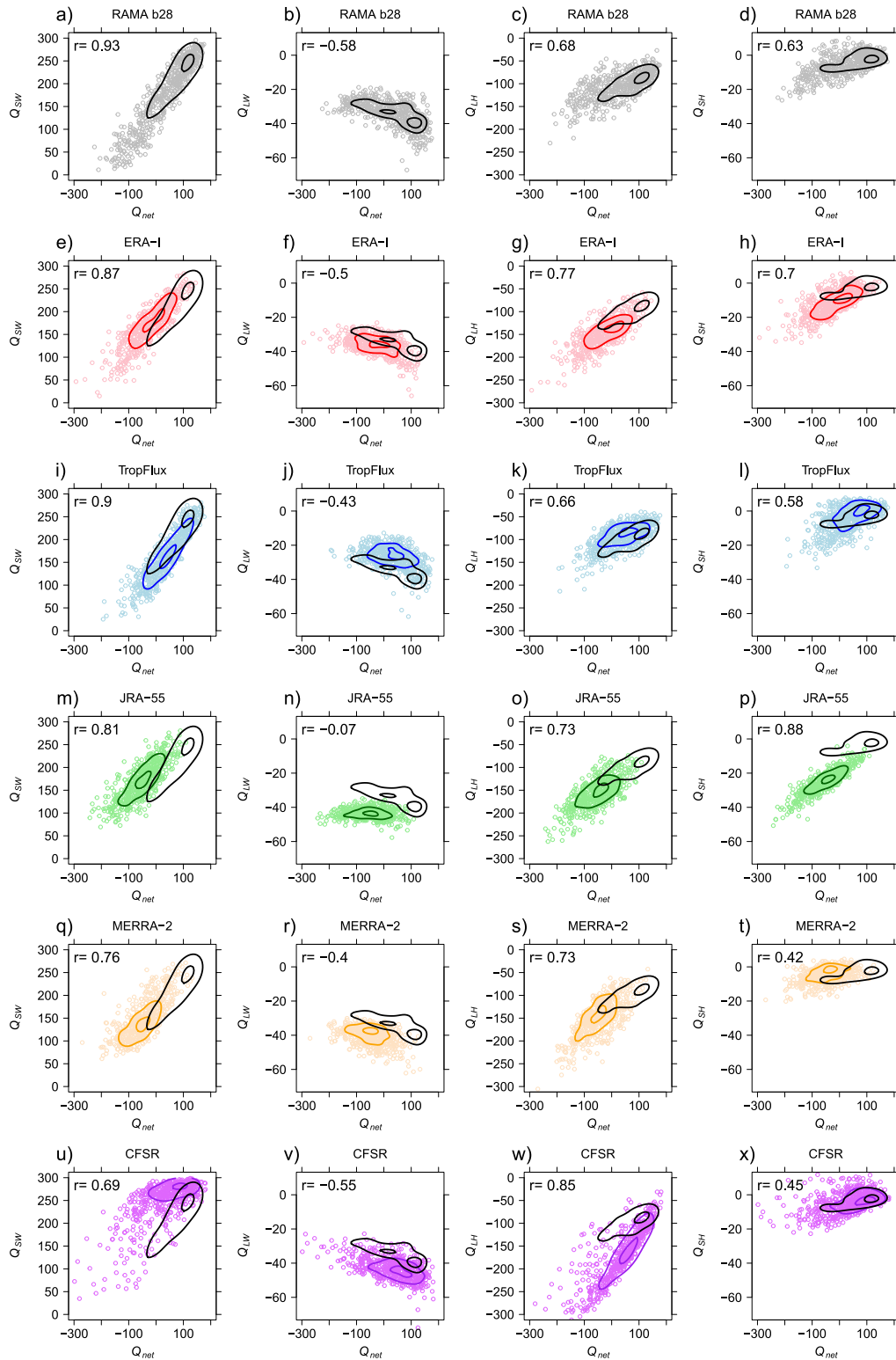
FIG. 3. Scatterplots for Q_{net} vs each of Q_{SW}, Q_{LW}, Q_{SH}, and Q_{LH} (W m^{-2}) from (a)–(d) RAMA buoy observations, (e)–(h) ERA-I, (i)–(l) TropFlux, (m)–(p) JRA-55, (q)–(t) MERRA-2, and (u)–(x) CFSR at site b28 (8°N, 90°E). Contours enclose 10% and 50% of the points in each joint distribution. RAMA contours (black) are repeated for comparison in (e)–(x).
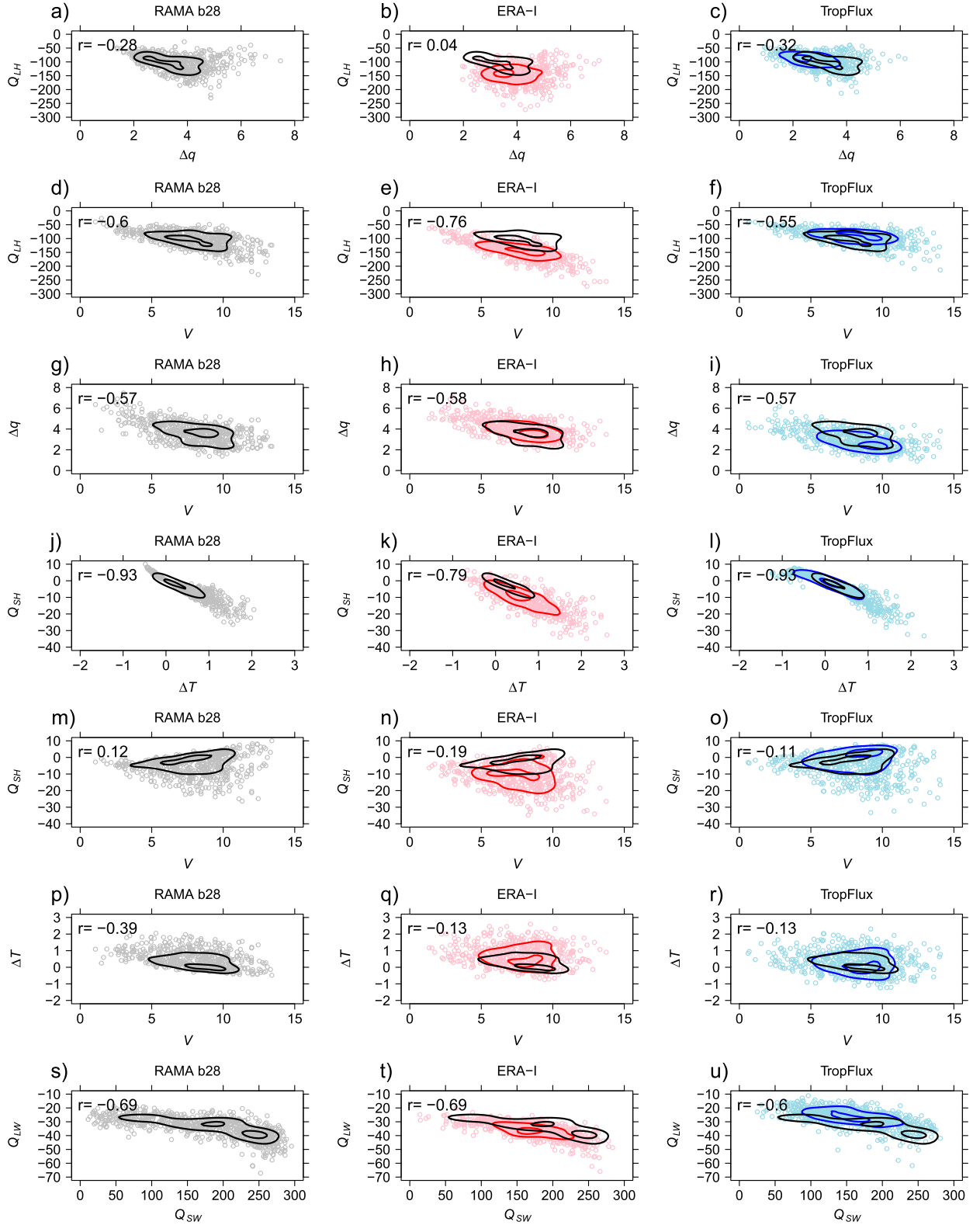
FIG. 4. Scatterplots of (a)–(c) Q_{LH} (W m^{-2}) vs Δq (g kg^{-1}), (d)–(f) Q_{LH} (W m^{-2}) vs V (m s^{-1}), (g)–(i) Δq (g kg^{-1}) vs V (m s^{-1}), (j)–(l) Q_{SH} (W m^{-2}) vs ΔT (°C), (m)–(o) Q_{SH} (W m^{-2}) vs V (m s^{-1}), (p)–(r) ΔT (°C) vs V (m s^{-1}), and (s)–(u) Q_{LW} (W m^{-2}) vs Q_{SW} (W m^{-2}) from (left) RAMA buoy observations, (center) ERA-I, and (right) TropFlux at site b28 (8°N, 90°E). Contours enclose 10% and 50% of the points in each joint distribution. RAMA contours (black) are repeated for comparison in the ERA-I and TropFlux panels.
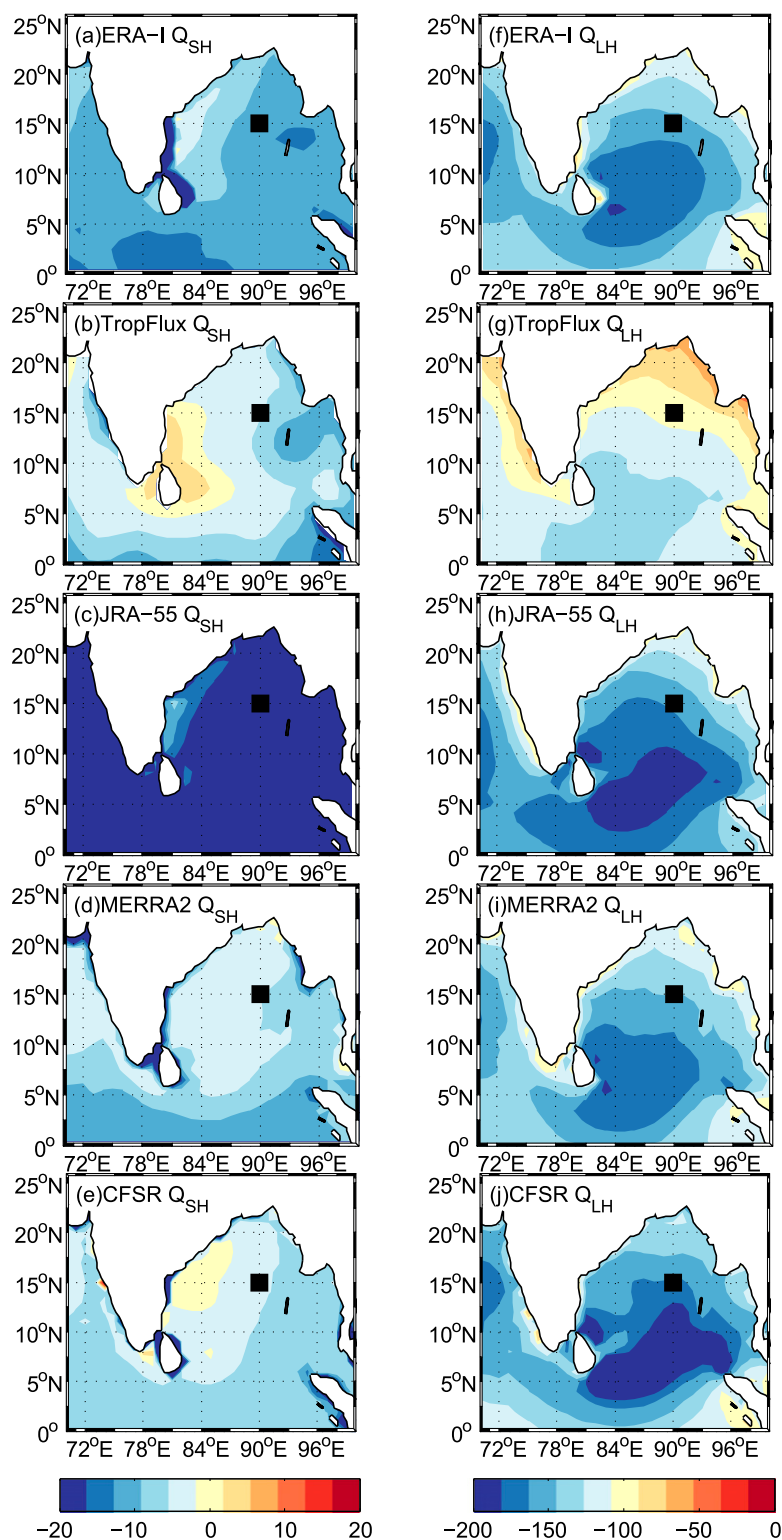
FIG. 5. (a)–(e) Mean Q_{SH} (W m^{-2}) and (f)–(j) Q_{LH} (W m^{-2}) for (a),(f) ERA-I, (b),(g) TropFlux, (c),(h) JRA-55, (d),(i) MERRA-2, and (e),(j) CFSR. All fields are averaged for the SW monsoon season (JJAS) from 2007 to 2015. The black square indicates the location of the RAMA buoy b28, in the BoB.

ERA-I, and CFSR show a larger gradient decreasing from east to west across the buoy, and MERRA-2 and JRA-55 show almost no gradient. Other spatial differences are apparent in the patterns across coastal waters of the BoB, such as the region around Sri Lanka and the east coast of India, where only TropFlux and CFSR show regions of positive Q_{SH} (i.e., heat gain to the ocean). (We note the smaller contour range in Q_{SH} values from -20 to $20\,W\,m^{-2}$, cf. Q_{LH} from -200 to $0\,W\,m^{-2}$). For the mean Q_{LH} field, all products show a region of strong Q_{LH} centered on the southern part of the BoB, sandwiched between the equator and 10°N, covering the zonal extent of the basin. This pool of elevated Q_{LH} in the southern BoB appears largest and strongest in JRA-55 and CFSR, and in TropFlux the pool is shifted farther south and is considerably weaker compared to the remaining reanalysis products. Near b28 most products show a strong gradient in Q_{LH} decreasing from south to north, although in JRA-55 this gradient is slightly more sloped in the southwest–northeast direction. These patterns are consistent with the mean and standard deviation of the Q_{SH} and Q_{LH} from all products (Fig. S3 in the supplemental material). Combining these results with the biases and skill scores from section 3, where it was shown that Q_{LH} from TropFlux underestimates the observed Q_{LH} at b28 and the reanalysis products all overestimate the observed Q_{LH} by a wide margin on the order of 50–75 $W\,m^{-2}$, suggests TropFlux captures turbulent fluxes best, and the erroneously enhanced Q_{LH} seen at the b28 location in ERA-I, JRA-55, MERRA-2, and CFSR shows large-scale coherence across the BoB.

In section 3, Q_{SW} was shown to have some of the largest biases in the reanalysis products when compared with the in situ Q_{SW} from RAMA buoy b28 data. It follows that in Fig. 6, the mean Q_{SW} fields over the BoB show a wide range in Q_{SW} values ($\sim$100–250 $W\,m^{-2}$), differing quite substantially between products: CFSR and MERRA-2 show higher and lower values, respectively, of Q_{SW} when compared to ERA-I, TropFlux, and JRA-55. The mean Q_{SW} field across the BoB depicts regions of high Q_{SW} in the vicinity of Sri Lanka and southwest of the southernmost tip of India in TropFlux and JRA-55, from the equator to 5°N in ERA-I, but not in the MERRA-2 or CFSR products, consistent with the dry slot in the rain shadow of Sri Lanka (Puvaneswaran and Smithson 1991). Since the smallest biases (which are negative) were observed in JRA-55 and ERA-I in section 3 (Fig. 2a), these results suggest TropFlux and (to a greater degree) MERRA-2 values are underestimating the observed Q_{SW} across the basin, while CFSR is overestimating them across the basin on an order of 70 $W\,m^{-2}$. CFSR also shows the greatest departure from

the spatial patterns across the BoB than any of the other products, failing to capture the region of high Q_{SW} around Sri Lanka and southeastern India (Fig. S3). The difference in the range of Q_{LW} values across products is considerably smaller, consistent with section 3, where it was shown that the Q_{LW} had some of the smallest biases among the flux components (Fig. 2a). The mean field for Q_{LW} appears to show a more consistent pattern in spatial gradients from all products across the BoB, compared to Q_{SW} (Figs. 6f–j). In general, there is a high–low (south–north) gradient in Q_{LW} across the BoB.

The parameter Q_{net} for ERA-I, JRA-55, and MERRA-2 depicts large heat loss in the central and southern regions of the BoB (Fig. S4 in the supplemental material), which is consistent with the results shown in section 3 (Fig. 2). TropFlux and CFSR, on the other hand, depict a net heat gain by the ocean all across the basin and strongest in the southwest and northern parts of the basin. In particular, values for Q_{net} in CFSR are the product of errors in the Q_{LH} and Q_{SW} components canceling out. Since the patterns of variability are generally similar across the basin for all products (Fig. 6), results from section 3 wherein TropFlux underestimates observed Q_{LW} and all remaining products overestimate the observed Q_{LW} at RAMA buoy b28 (Fig. 2a) are taken to be representative of the basinwide biases in the BoB.

b. Monsoon variability: The boreal summer intraseasonal oscillation

In the previous sections, the performance of the reanalysis products in simulating the day-to-day variability at a point location in the BoB (sections 3 and 4) and the time-mean spatial patterns over the BoB (section 5a) was assessed. Another necessary capability of a reanalysis product is that it should be able to simulate the main spatial and temporal patterns of variability within a given region, as these modes are the likely sources of potential predictability in a forecast system that uses reanalysis products as a forcing input. The boreal summer intraseasonal oscillation (BSISO) is one of the primary modes of variability associated with the Asian summer monsoon (Webster et al. 1998; Lee et al. 2013). The BSISO is also known as the monsoon intraseasonal oscillation (MISO) (Suhas et al. 2013), and was first identified as northward-propagating 30–60-day bands of clouds and convection over India by, for example, Sikka and Gadgil (1980). It is often recognized as the northern summer counterpart to the Madden–Julian oscillation (MJO) (Madden and Julian 1994). Here the BSISO index from Lee et al. (2013) is used to assess the representation of boreal summer intraseasonal variability from the reanalysis products.
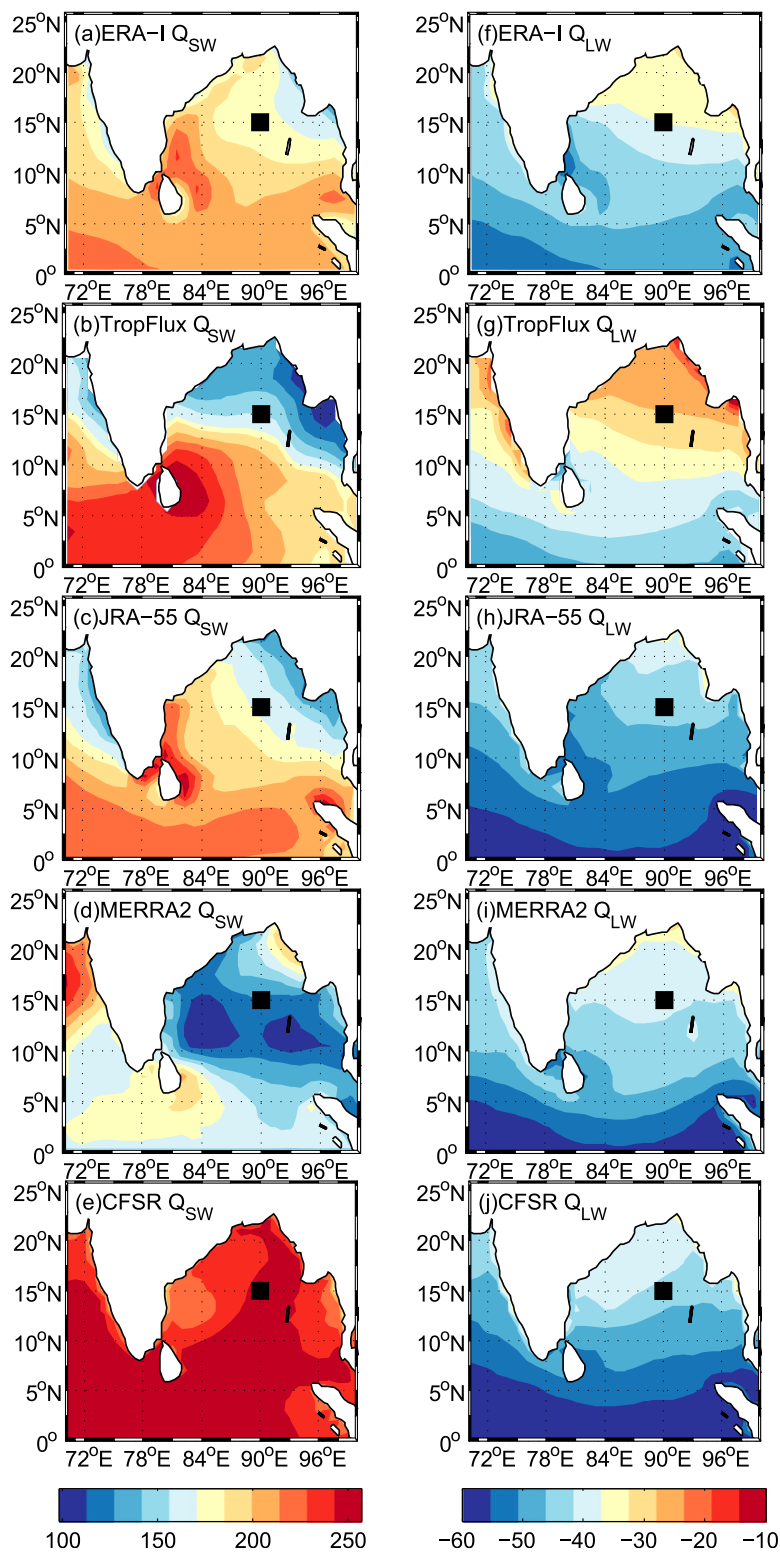
FIG. 6. As in Fig. 5 but for Q_{SW} and Q_{LW}.

Similar to the MJO (Wheeler and Hendon 2004), the BSISO indices are constructed from multivariate empirical orthogonal function analysis of satellite OLR and the 850-hPa zonal wind fields from NCEP–DOE AMIP-II reanalysis in the region of the Asian summer monsoon (Lee et al. 2013). The first two principal components (PCs) of the BSISO form the BSISO1, which corresponds to the northward propagating component of the summer monsoon and has a 30–60-day period (Wang et al. 2005). The third and fourth PC of the BSISO form the BSISO2, which is the northward or northwestward component of the monsoon, usually associated with the premonsoon and monsoon onset periods, and has a period of 10–20 days (Kikuchi and Wang 2010). Here we focus on the 30–60-day northward propagating BSISO, that is, the BSISO1.

The BSISO1 mode is divided into eight phases, each phase covering one-eighth of the cycle (Lee et al. 2013). During phase 1, a zonally elongated band of enhanced atmospheric convection lies over the equatorial Indian Ocean, while a band of suppressed convection extends from India southeastward across the BoB, Southeast Asia, and into the equatorial western Pacific (Fig. 7). Over phases 2, 3, and 4, the band of enhanced convection moves northward and eastward, while the suppressed convection retreats to the northeast and contracts. A second band of suppressed convection then starts to develop over the equatorial Indian Ocean, such that the anomalies at phase 5 are approximately the opposite sign to those at phase 1 (a half-cycle earlier). The new band of suppressed convection then propagates northeastward during phases 6, 7, and 8. Finally, enhanced convection reestablishes itself over the equatorial Indian Ocean again in phase 1, and the next cycle begins.

The BSISO1 composites here are constructed using an index of BSISO1 phases 1–8 based on satellite OLR and 850-hPa zonal wind fields as described in Lee et al. (2013) [available through the Asian–Pacific Economic Cooperation (APEC) Climate Center data portal; http://www.apcc21.net/ser/casts.do?lang=en]. For each variable V, wind direction, Q_{SW}, Q_{LH}, and Q_{net}, daily anomalies were computed from the monthly mean for JJAS 2007–15. Then, each day during the study period was allocated to one of the eight BSISO1 phases or was discarded if the overall BSISO1 amplitude was weak [i.e., $(PC1^2 + PC2^2)^{1/2} < 1$]. Data from each product were averaged over the days in each phase to obtain the eight phase composites of the life cycle.

The BSISO1 representations in each reanalysis product are first validated against the in situ data at the RAMA buoy b28 location. Figure 8 shows the median, interquartile range, 95% confidence intervals, and outliers for V, wind direction, Q_{SW}, Q_{LH}, and Q_{net} from the

in situ data and the ERA-I, TropFlux, and CFSR products at each phase of the BSISO1 life cycle. During phase 1 (phase 2) all products overestimate (underestimate) the observed BSISO1 V and, in general, all do a reasonable job of capturing the observed V during BSISO1 phases 3–8 (Figs. 8a–d). The prevailing surface winds remain approximately from the southwest during JJAS, as measured by the buoy and in all the products at the buoy location (Figs. 8e–h). The change in surface wind direction through the cycle is less well represented in the products. During phases 1–3, the buoy shows winds becoming more southerly, whereas all of the products show a change to more westerly winds during these phases.

The RAMA Q_{SW} measurements show high median values in phases 1–3 (Fig. 8i), during the convectively suppressed part of the BSISO1 cycle in the northern BoB (Fig. 7). As the enhanced convection moves into the BoB, cloud cover increases and the Q_{SW} values decrease during phases 4, 5, and 7. Although the reanalysis products do reproduce this qualitative pattern, they all underestimate the amplitude of the Q_{SW} variability associated with the BSISO1 (Figs. 8j–l). In particular, ERA-I and TropFlux tend to underestimate (overestimate) highs (lows) in the observed Q_{SW} within a range of $\pm 45\,\mathrm{W\,m^{-2}}$; meanwhile, although CFSR also generally underestimates the amplitude of the variability, it grossly overestimates Q_{SW} values (associated with BSISO1) in comparison with the observed Q_{SW}, with up to values of $75\,\mathrm{W\,m^{-2}}$. These results are consistent with section 3, where it was shown that ERA-I and (to a lesser degree) TropFlux reasonably estimated the observed Q_{SW} based on skill score; and CFSR showed large positive biases, low correlation, and poor skill score for Q_{SW}. Hence, in an ocean model forced by one of these products, the heating of the ocean surface by Q_{SW} during the suppressed convective phase and the cooling during the active convective phase of the BSISO1 would both be severely misrepresented.

The systematic error apparent in Q_{SW} is compensated to a certain degree by a systematic error in Q_{LH} of similar magnitude (Figs. 8n–p). The Q_{LH} at the RAMA buoy b28 location shows low median Q_{LH} values in phases 1–3, indicating reduced cooling of the ocean surface, and higher Q_{LH} values from phases 5–7, indicating increased cooling of the ocean surface (Fig. 8m). The TropFlux product does best at capturing the Q_{LH} BSISO1 variability and magnitude. The other data products appear to generally capture the observed variability correctly; however, both ERA-I and (to a greater extent) CFSR largely overestimate the median values of the observed Q_{LH}, indicating erroneously high cooling of the ocean surface. The significantly reduced
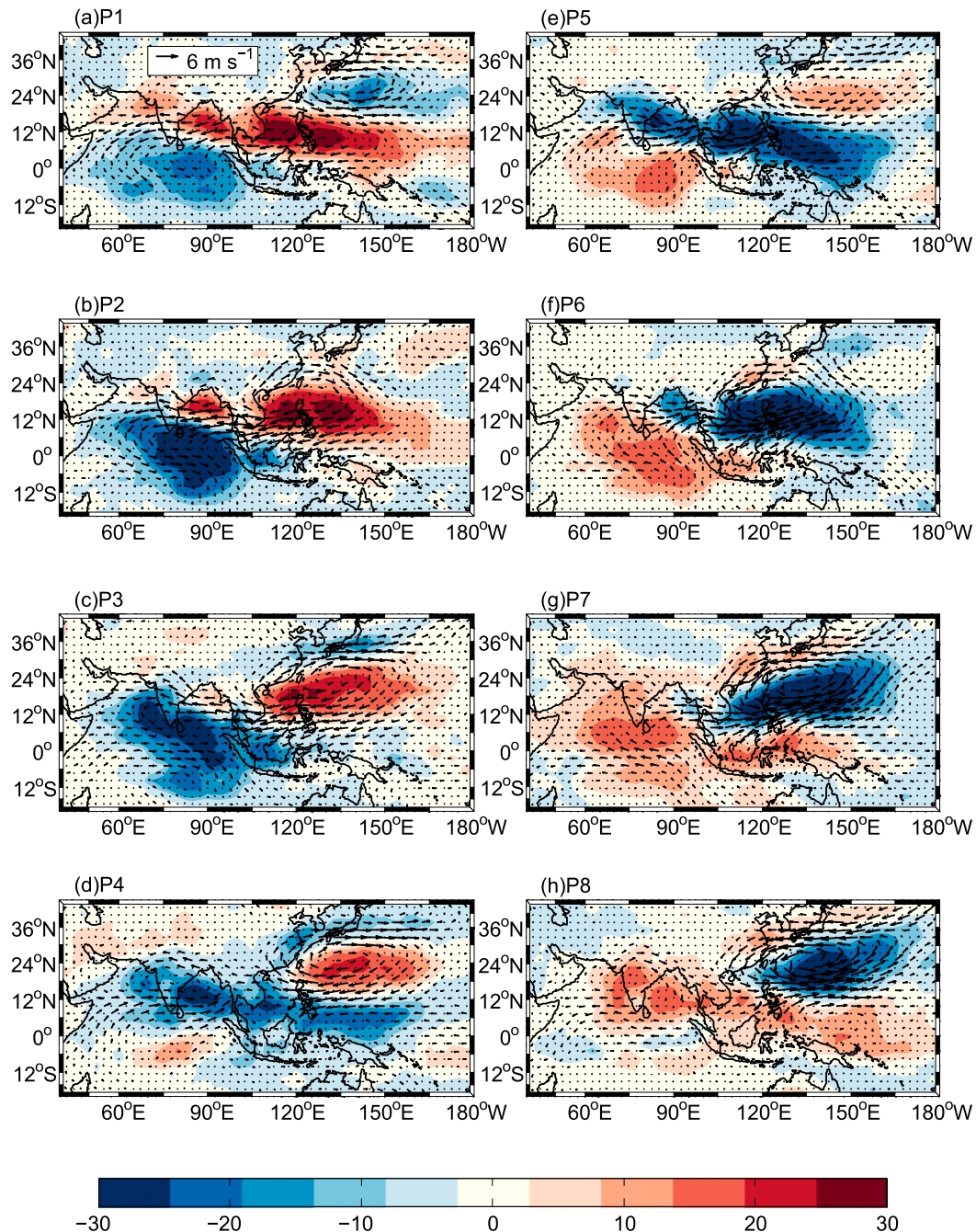
FIG. 7. BSISO1 life-cycle composite of NOAA OLR anomalies (shaded; W m^{-2}) and NCEP–DOE 850-hPa wind anomalies (vectors; m s^{-1}).

bias in Q_{net} from CFSR throughout all phases (Fig. 8t) indicates the systemic error in Q_{SW} is being largely compensated for by the systemic error in Q_{LH}. Hence, in the case of CFSR and (to a much smaller extent) TropFlux, the erroneous strong cooling of the ocean surface from high Q_{LH} values offsets the erroneous high heating of the ocean surface from the Q_{SW} values.

ERA-I generally captures the observed BSISO1 Q_{net} variability; however, the Q_{SW} and Q_{LH} offsets add up and yield a Q_{net} with a sign opposite to the observed, consistent with Fig. 2.

ERA-I has a similar pattern of Q_{SW} and Q_{LH} biases, but the magnitude of errors is smaller in comparison to CFSR. The blended product, TropFlux, shows similar
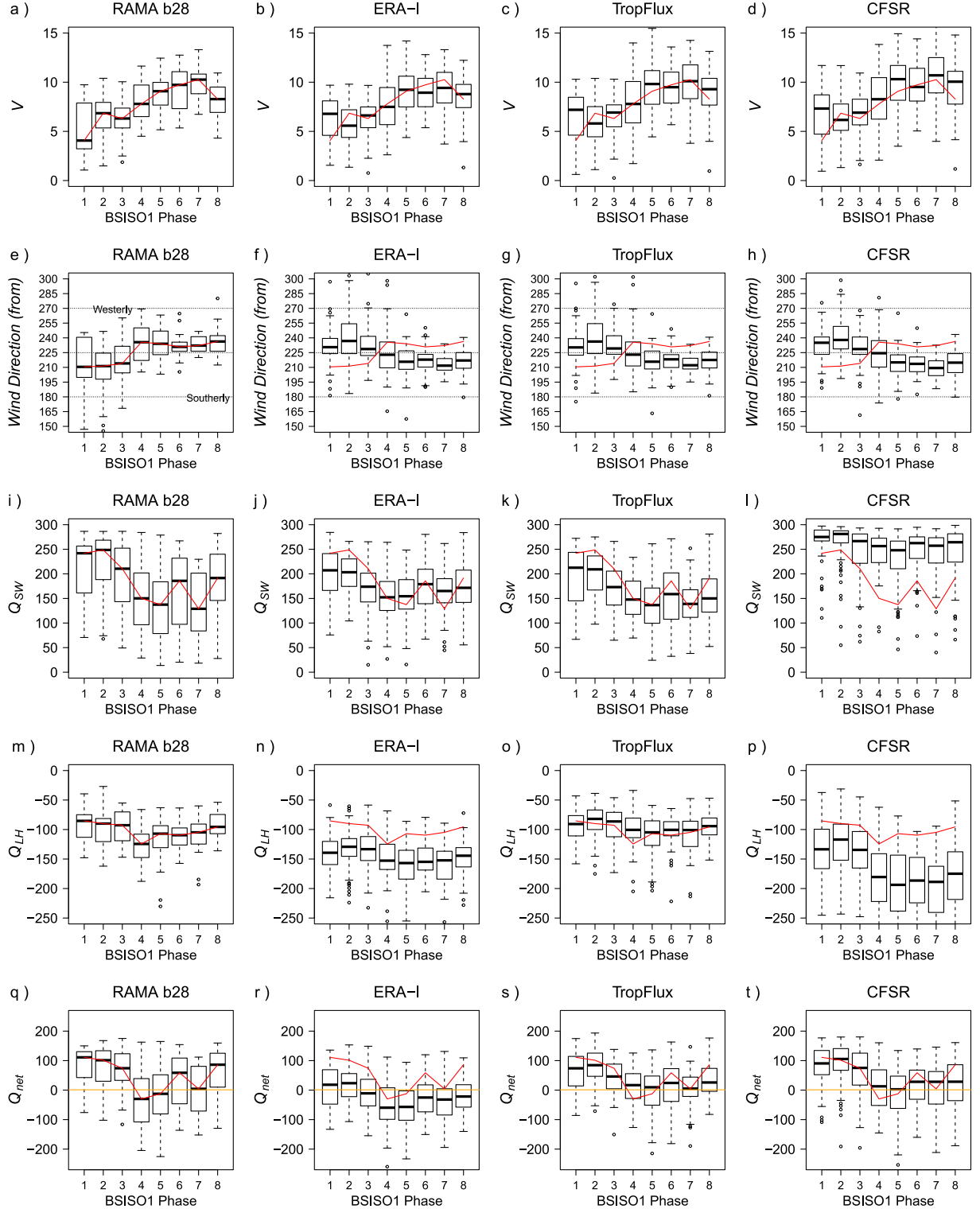
FIG. 8. Median, interquartile range, 95% confidence interval, and outliers for V (m s^{-1}), wind direction (°), Q_{SW} (W m^{-2}), Q_{LH} (W m^{-2}), and Q_{net} (W m^{-2}) vs BSISO1 phases 1–8 from (a),(e),(i),(m),(q) RAMA buoy b28; (b),(f),(j),(n),(r) ERA-I; (c),(g),(k),(o),(s) TropFlux; and (d),(h),(l),(p),(t) CFSR. The red line is the RAMA buoy b28 median line repeated for comparison in the ERA-I, TropFlux, and CFSR panels.

offsets in the Q_{SW}; however, its Q_{LH} and Q_{net} are more realistic and appear to capture best of the observed BSISO1 Q_{SW} and Q_{LH} variability. These results are consistent with section 3, where it was showed that in general ERA-I does better at capturing radiative fluxes and TropFlux captures turbulent and net heat fluxes best. To calculate Q_{SW}, TropFlux uses observed cloudiness data from ISCCP up until 2009 (when it was last available) and the ISCCP mean seasonal cycle and NOAA OLR thereafter (KP12), whereas the four reanalysis products use their internally generated cloud fields, which are dependent on their convective and microphysical parameterization schemes. This highlights the well-known major errors in these schemes (e.g., Boilley and Wald 2015). These errors clearly impact intraseasonal variability as well as the mean fields.

Figure 9 shows composites of daily anomalies from the monthly mean for JJAS from 2007 to 2015 for Q_{SW}, Q_{LH}, V, and q_a during the most extreme phases (phases 2 and 5) of the BSISO1 life cycle over the BoB from TropFlux (shaded) and ERA-I (contours). During phase 2, both products depict large positive Q_{SW} anomalies in the northern BoB, and negative Q_{LH} and V anomalies in the eastern BoB (Figs. 9a–c), indicating clear skies and suppressed convection in that region. In phase 5, the anomalies have flipped sign, and there is an elongated zonal band of negative Q_{SW} anomalies and positive Q_{LH} and V anomalies across the BoB, indicating enhanced convection, in agreement with the BSISO1 life cycle from NOAA OLR and NCEP–DOE wind fields (Fig. 7) and the BSISO1 life cycle at the RAMA buoy b28 location (Fig. 8). Generally, both TropFlux and ERA-I consistently capture the correct patterns of variability associated with the BSISO1 at phases 2 and 5 (see Fig. 7). However, ERA-I shows weaker Q_{SW} anomalies and stronger Q_{LH} anomalies than TropFlux, consistent with results observed at the RAMA buoy b28 location that suggest TropFlux is more accurate at this location (Fig. 8).

In contrast, the BSISO1 life cycles of Q_{SW} and Q_{LH} in JRA-55, MERRA-2, and CFSR are shown to be noisier (Fig. 10) than their counterparts in TropFlux and ERA-I, especially during phase 5. During phase 5, usually characterized by a zonal band of enhanced convection in the northern BoB, JRA-55 only captures a weakened band of negative Q_{SW} anomalies in the northernmost and easternmost parts of the BoB (Fig. 10d). In MERRA-2, the BSISO1 signal is barely perceptible from the Q_{SW}, and in CFSR the band of Q_{SW} variability is weakened and shifted south (Figs. 10e,f). CFSR further shows exaggeratedly high positive Q_{LH} anomalies that compensate for the Q_{SW} bias. The diminished Q_{SW} variability in MERRA-2 can likely be attributed to the

MERRA-2 negative bias, low correlation, and poor skill score in Q_{SW} (Fig. 2). The difficulties of MERRA-2, JRA-55, and CFSR in capturing the BSISO1 signal across the basin is consistent with their difficulties capturing the BSISO1 variability at RAMA buoy b28 (Fig. 8) and can be directly attributed to the products' difficulties in representing surface fluxes, as seen in the previous sections (i.e., sections 3 and 4). In general, TropFlux and ERA-I captured the observed BSISO1 Q_{SW} best, and TropFlux captured the observed BSISO1 Q_{LH} and Q_{net} best; both products depicted a life-cycle composite that was encouragingly similar to the Lee et al. (2013) OLR life cycle (Fig. 8).

Finally, we note that with low wind speeds and high radiation, the effectiveness of the radiation shields on the T_a and humidity sensor decreases (Anderson and Baumgartner 1998). Anderson and Baumgartner (1998) estimated that for naturally ventilated sensors, errors of up to 3.4°C in the mean daytime temperature could lead to biases of 22 W m^{-2} in the turbulent fluxes. Here the T_a and humidity sensor aboard the ATLAS moorings used multiplate radiation shields and are naturally ventilated, hence high radiation and low wind speeds may result in less effective shielding (Freitag et al. 2001). Specifically, manufacturer estimates that for radiation above 1080 W m^{-2} and winds at or below 3 m s^{-1}, the temperature bias can increase from 0.2° to 0.4°C (Freitag et al. 2001). During phase 1 of the BSISO1, when wind speeds drop to 3 m s^{-1} and the solar radiation is quite high as a result of suppressed convection, there are greater chances of T_a errors occurring because of poor shielding. However, careful examination of the T_a anomalies per phase (not shown here) suggests there are no significant T_a errors. The high wind speed during the majority of the phases (2–8) decreases the chances of radiation shields contributing to the overall error.

6. Summary and conclusions

In this study, five data products are analyzed and compared with in situ data from a moored array in the BoB to determine how well the reanalysis products characterize air–sea fluxes and intraseasonal variability during the SW monsoon season. Specifically, meteorological parameters, SST, V, T_a, and q_a, air–sea temperature difference ΔT, air–sea humidity difference Δq, and fluxes, Q_{SW}, Q_{LW}, Q_{SH}, Q_{LH}, and Q_{net} from ERA-I, TropFlux, JRA-55, MERRA-2, and CFSR were evaluated for JJAS from 2007–15, and compared with in situ data from the RAMA surface flux reference site at 15°N, 90°E, denoted b28. In general, most products did reasonably well at representing the meteorological variables, although q_a had the lowest correlations, highest
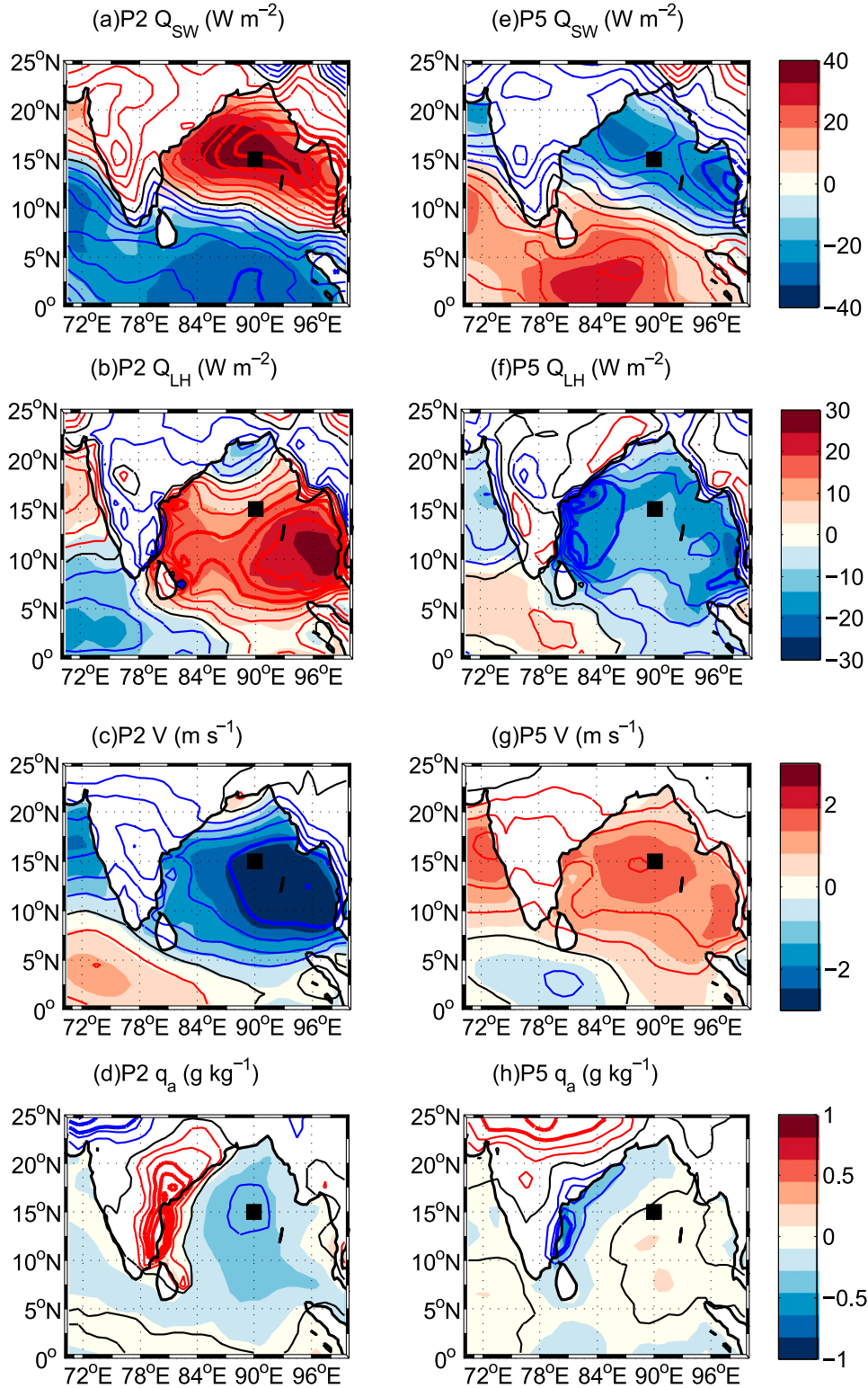
FIG. 9. Composite of phases (a)–(d) 2 and (e)–(h) 5 of the BSISO1 life cycle. TropFlux (shaded) and ERA-I (contours) of Q_{SW} anomalies at phase 2 in (a) and 5 in (e); Q_{LH} anomalies at phase 2 in (b) and 5 in (f); V anomalies at phase 2 in (c) and 5 in (g); and q_a anomalies at phase 2 in (d) and 5 in (h). ERA-I Q_{SW} contours range from -40 to 40 W m^{-2} and Q_{LH} contours range from -30 to 30 W m^{-2}, with 5 W m^{-2} contour interval. ERA-I V contours range from -3 to 3 m s^{-1}, with 0.5 m s^{-1} contour interval. ERA-I q_a contours range from -1 to 1 g kg^{-1}, with 0.2 g kg^{-1} contour interval. The black square indicates the location of the RAMA buoy b28.
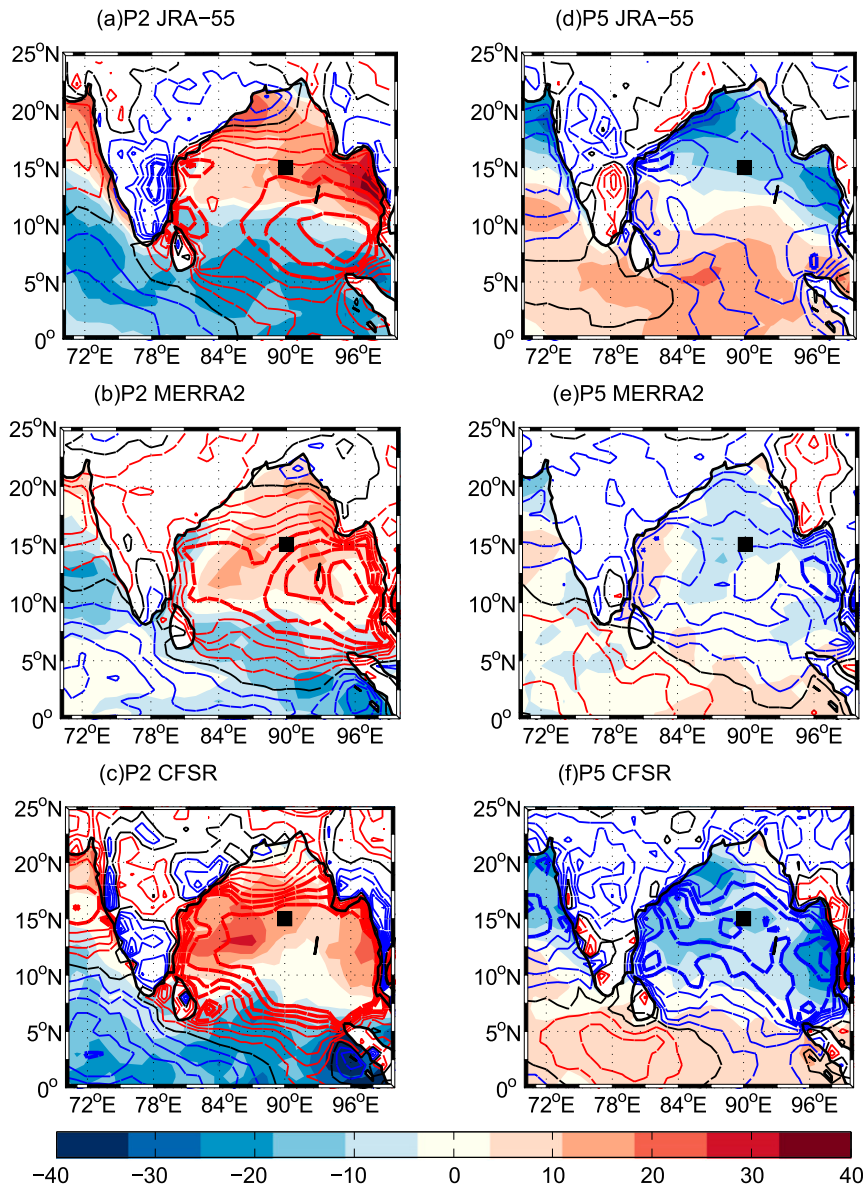
FIG. 10. Phases (a)–(c) 2 and (d)–(f) 5 of the Q_{SW} (shaded) and Q_{LH} (contours) anomalies (W m^{-2}) from (a),(d) JRA-55, (b),(e) MERRA-2, and (c),(f) CFSR based on the BSISO1 phases. The Q_{LH} contours range from -40 to 40 W m^{-2}, with 5 W m^{-2} contour interval. The black square indicates the location of the RAMA buoy b28.

biases, and lowest skill scores across all products (Fig. 2). TropFlux and ERA-I performed best, while the coupled product, CFSR, exhibited some of the largest biases. From the flux variables, Q_{SW} and Q_{LH} were shown to be the main drivers of the observed Q_{net} variability, but were also the two variables the products had the most difficulty capturing. Correlations were lowest for the radiative fluxes and Q_{SH}, and there were nonnegligible biases in the range of 50 W m^{-2} in Q_{SW}. For Q_{LH}, all products other than TropFlux overestimated the observed Q_{LH} by at least 40 W m^{-2}, while the TropFlux

bias was approximately 10 W m^{-2}. In general, based on mean biases, correlations, and skill scores, ERA-I was shown to capture radiative fluxes best, while TropFlux better captured turbulent and latent heat fluxes. Skill scores indicated poor performance for Q_{LH} and the radiative fluxes in MERRA-2 and CFSR, and we note that for the coupled ocean–atmosphere product CFSR, these biases canceled each other out in the Q_{net}.

The temporal-mean fields for the fluxes across the BoB were investigated in section 5a, where various discrepancies were observed in the spatial patterns

among the products. For Q_{SH}, the patterns were consistent across ERA-I, TropFlux, and CFSR, although JRA-55 and ERA-I had large negative biases, indicating erroneously high heat loss to the atmosphere and therefore erroneous cooling of the sea surface. Patterns of Q_{LH} variability were generally consistent across all products (i.e., a region of high Q_{LH} in the southwest corner of the BoB), although values ranged on the order of 40 W m^{-2} between the reanalysis products. For Q_{SW}, ERA-I outperformed the other three products by a wide margin (CFSR, in particular, showed much higher values and different spatial gradients than the other products). Differences in Q_{LH} and Q_{SW} in the reanalysis products were generally attributed to differences or issues with the internally generated cloud fields and/or schemes (e.g., Wang et al. 2011; Boilley and Wald 2015). For Q_{LW}, even though spatial gradients were consistent, correlations high, and biases small, skill scores were low (except for ERA-I) across all products. In general, results from the temporal-mean field indicate that the results at the b28 location are not localized, and biases of similar magnitude to those seen at b28 will be widespread across the BoB. Further, the biases in the fluxes implied by the meteorological parameters at b28 are likely representative of the magnitude of biases observed in other regions in the basin in the temporally averaged fields.

The BSISO1 index, representative of the northward propagating component of the summer monsoon (with a 30–60-day periodicity), was used to test the ability of the different products to represent the principal mode of atmospheric variability in the BoB in this season, in particular in the representation of Q_{SW} and Q_{LH} in ERA-I, TropFlux, and CFSR. Comparison with RAMA buoy b28 suggested TropFlux and ERA-I most reliably captured surface flux variability compared with the observed BSISO1 Q_{SW} cycle at 15°N, 90°E; however, TropFlux captured the variability and magnitude of the observed Q_{LH} and Q_{net} best. The analysis of the mean fields, the comparison with BSISO1 at b28, and comparison with Lee et al. (2013) satellite OLR maps allows us to extend this confidence over the entire BoB. Thus, both TropFlux and ERA-I appear to best represent the variability of the surface fluxes at RAMA buoy b28 and across the entire BoB basin. Conversely, MERRA-2, CFSR, and JRA-55 struggled to capture the climatic variability associated with the BSISO1, with weak Q_{SW} variability at the location of RAMA buoy b28 suggesting that the convective signal is poorly represented in these products, while the overestimation of Q_{LH} variability suggests erroneous surface wind and humidity fields. Hence, we infer inability to accurately capture or reproduce the surface fluxes at b28 or at mean field

levels shows that the MERRA-2, CFSR, and JRA-55 products will similarly struggle to capture variability associated with the boreal summer monsoon.

As air–sea fluxes have been shown to be key players in monsoon variability (Vecchi and Harrison 2002), caution is advised when selecting a data product to represent monsoonal processes. This study has highlighted significant and critical deficiencies in reanalysis flux products from the accumulated errors observed in the meteorological parameters and surface fluxes specific to the southwest monsoon time period and have yet to be verified for the entire seasonal cycle. In general, ERA-I and TropFlux were shown to outperform MERRA-2, JRA-55, and CFSR; ERA-I represented radiative fluxes best, while TropFlux better captured turbulent and net heat fluxes. Based on findings shown here, this analysis recommends TropFlux and ERA-I as the best available products for the study of air–sea fluxes and intraseasonal variability over the BoB during the SW monsoon, or for the forcing of ocean models during boreal summer in the tropical Indian Ocean.

Physical Sciences Division (PSD), Boulder, Colorado, from their website (http://www.cdc.noaa.gov). The BSISO data were provided by the APEC Climate Center through their website (http://www.apcc21.net/ser/moni.do?lang=en). The authors are grateful to Dr. Shoji Hirahara of JMA for the JRA-55 daily SST data. The MATLAB version of the COARE3.0 algorithm was used to estimate the uncertainty in the RAMA turbulent fluxes (ftp://ftp.etl.noaa.gov/BLO/Air-Sea/bulkalg/cor3–0). The authors are also grateful for the helpful insight and comments from three anonymous reviewers.

REFERENCES

Anderson, S. P., and M. F. Baumgartner, 1998: Radiative heating errors in naturally ventilated air temperature measurements made from buoys. *J. Atmos. Oceanic Technol.*, **15**, 157–173, https://doi.org/10.1175/1520-0426(1998)015<0157:RHEINV>2.0.CO;2.

Berrisford, P., P. Kållberg, S. Kobayashi, D. Dee, S. Uppala, A. J. Simmons, P. Poli, and H. Sato, 2011: Atmospheric conservation properties in ERA-Interim. *Quart. J. Roy. Meteor. Soc.*, **137**, 1381–1399, https://doi.org/10.1002/qj.864.

Boilley, A., and L. Wald, 2015: Comparison between meteorological re-analyses from ERA-Interim and MERRA and measurements of daily solar irradiation at surface. *Renew. Energy*, **75**, 135–143, https://doi.org/10.1016/j.renene.2014.09.042.

Bolker, B. M., 2008: *Ecological Models and Data in R*. Princeton University Press, 408 pp.

Bolton, D., 1980: The computation of equivalent potential temperature. *Mon. Wea. Rev.*, **108**, 1046–1053, https://doi.org/10.1175/1520-0493(1980)108<1046:TCOEPT>2.0.CO;2.

Bosilovich, M. G., and Coauthors, 2015: MERRA-2: Initial evaluation of the climate. NASA Tech. Memo. NASA/TM-2015-104606/Vol. 43, 145 pp., https://gmao.gsfc.nasa.gov/pubs/docs/Bosilovich803.pdf.

Brunke, M. A., Z. Wang, X. Zeng, M. Bosilovich, and C.-L. Shie, 2011: An assessment of the uncertainties in ocean surface turbulent fluxes in 11 reanalysis, satellite-derived, and combined global datasets. *J. Climate*, **24**, 5469–5493, https://doi.org/10.1175/2011JCLI4223.1.

Cronin, M. F., C. W. Fairall, and M. J. McPhaden, 2006: An assessment of buoy-derived and numerical weather prediction surface heat fluxes in the tropical Pacific. *J. Geophys. Res.*, **111**, C06038, https://doi.org/10.1029/2005JC003324.

Dee, D. P., and S. Uppala, 2009: Variational bias correction of satellite radiance data in the ERA-Interim reanalysis. *Quart. J. Roy. Meteor. Soc.*, **135**, 1830–1841, https://doi.org/10.1002/qj.493.

——, and Coauthors, 2011: The ERA-Interim reanalysis: Configuration and performance of the data assimilation system. *Quart. J. Roy. Meteor. Soc.*, **137**, 553–597, https://doi.org/10.1002/qj.828.

DeMott, C. A., C. Stan, D. A. Randall, and M. D. Branson, 2014: Intraseasonal variability in coupled GCMs: The roles of ocean feedbacks and model physics. *J. Climate*, **27**, 4970–4995, https://doi.org/10.1175/JCLI-D-13-00760.1.

Donlon, C. J., M. Martin, J. Stark, J. Roberts-Jones, E. Fiedler, and W. Wimmer, 2012: The Operational Sea Surface Temperature and Sea Ice Analysis (OSTIA) system. *Remote Sens. Environ.*, **116**, 140–158, https://doi.org/10.1016/j.rse.2010.10.017.

Duncan, B., and W. Han, 2009: Indian Ocean intraseasonal sea surface temperature variability during boreal summer: Madden-Julian oscillation versus submonthly forcing and processes. *J. Geophys. Res.*, **114**, C05002, https://doi.org/10.1029/2008JC004958.

Fairall, C. W., E. F. Bradley, J. E. Hare, A. A. Grachev, and J. B. Edson, 2003: Bulk parameterization of air–sea fluxes: Updates and verification for the COARE algorithm. *J. Climate*, **16**, 571–591, https://doi.org/10.1175/1520-0442(2003)016<0571:BPOASF>2.0.CO;2.

Freitag, H. P., M. O'Haleck, G. C. Thomas, and M. J. McPhaden, 2001: Calibration procedures and instrumental accuracies for ATLAS wind measurements. NOAA Tech. Memo. OAR PMEL-119, 20 pp.

Girishkumar, M. S., J. Joseph, V. P. Thangaprakash, V. Pottapinjara, and M. J. McPhaden, 2017: Mixed layer temperature budget for the northward propagating summer monsoon intraseasonal oscillation (MISO) in the central Bay of Bengal. *J. Geophys. Res. Oceans*, **122**, 8841–8854, https://doi.org/10.1002/2017JC013073.

Goswami, B. B., M. Deshpande, P. Mukhopadhyay, S. K. Saha, S. A. Rao, R. Murthugudde, and B. N. Goswami, 2014: Simulation of monsoon intraseasonal variability in NCEP CFSv2 and its role on systematic bias. *Climate Dyn.*, **43**, 2725–2745, https://doi.org/10.1007/s00382-014-2089-5.

Goswami, B. N., 2012: South Asian monsoon. *Intraseasonal Variability in the Atmosphere-Ocean Climate System*, W. K.-M. Lau and D. E. Waliser, Eds., Springer, 21–72.

Ishii, M., A. Shouji, S. Sugimoto, and T. Matsumoto, 2005: Objective analyses of sea-surface temperature and marine meteorological variables for the 20th century using ICOADS and the Kobe collection. *Int. J. Climatol.*, **25**, 865–879, https://doi.org/10.1002/joc.1169.

Kikuchi, K., and B. Wang, 2010: Formation of tropical cyclones in the northern Indian Ocean associated with two types of tropical intraseasonal oscillation modes. *J. Meteor. Soc. Japan*, **88**, 475–496, https://doi.org/10.2151/jmsj.2010-313.

Kobayashi, S., and Coauthors, 2015: The JRA-55 reanalysis: General specifications and basic characteristics. *J. Meteor. Soc. Japan*, **93**, 5–48, https://doi.org/10.2151/jmsj.2015-001.

Kumar, B. P., J. Vialard, M. Lengaigne, V. S. N. Murty, and M. J. Mcphaden, 2012: TropFlux: Air-Sea Fluxes for the global tropical oceans—Description and evaluation. *Climate Dyn.*, **38**, 1521–1543, https://doi.org/10.1007/s00382-011-1115-0.

Lee, J.-Y., B. Wang, M. C. Wheeler, X. Fu, D. E. Waliser, and I.-S. Kang, 2013: Real-time multivariate indices for the boreal summer intraseasonal oscillation over the Asian summer monsoon region. *Climate Dyn.*, **40**, 493–509, https://doi.org/10.1007/s00382-012-1544-4.

Madden, R. A., and P. R. Julian, 1994: Observations of the 40–50-day tropical oscillation—A review. *Mon. Wea. Rev.*, **122**, 814–837, https://doi.org/10.1175/1520-0493(1994)122<0814:OOTDTO>2.0.CO;2.

McPhaden, M. J., and Coauthors, 2009: RAMA: The research moored array for African–Asian–Australian monsoon analysis and prediction. *Bull. Amer. Meteor. Soc.*, **90**, 459–480, https://doi.org/10.1175/2008BAMS2608.1.

——, and Coauthors, 2010: The Global Tropical Moored Buoy Array. *Proc. OceanObs'09: Sustained Ocean Observations and Information for Society Conf.*, Venice, Italy, European Space Agency, https://doi.org/10.5270/OceanObs09.cwp.61.

Murphy, A. H., 1988: Skill scores based on the mean square error and their relationships to the correlation coefficient. *Mon. Wea. Rev.*, **116**, 2417–2424, https://doi.org/10.1175/1520-0493(1988)116<2417:SSBOTM>2.0.CO;2.

Onogi, K., and Coauthors, 2007: The JRA-25 Reanalysis. *J. Meteor. Soc. Japan*, **85**, 369–432, https://doi.org/10.2151/jmsj.85.369.

Parampil, S. R., A. Gera, M. Ravichandran, and D. Sengupta, 2010: Intraseasonal response of mixed layer temperature and salinity in the Bay of Bengal to heat and freshwater flux. *J. Geophys. Res.*, **115**, C05002, https://doi.org/10.1029/2009JC005790.

Puvaneswaran, K. M., and P. A. Smithson, 1991: Precipitation–elevation relationships over Sri Lanka. *Theor. Appl. Climatol.*, **43**, 113–122, https://doi.org/10.1007/BF00867468.

R Core Team, 2015: R: A language and environment for statistical computing. R Foundation for Statistical Computing, https://www.r-project.org.

Rienecker, M. M., and Coauthors, 2011: MERRA: NASA's Modern-Era Retrospective Analysis for Research and Applications. *J. Climate*, **24**, 3624–3648, https://doi.org/10.1175/JCLI-D-11-00015.1.

Saha, S., and Coauthors, 2010: The NCEP Climate Forecast System Reanalysis. *Bull. Amer. Meteor. Soc.*, **91**, 1015–1057, https://doi.org/10.1175/2010BAMS3001.1.

——, and Coauthors, 2011: NCEP Climate Forecast System (CFSv2) 6-hourly products, version 2. NCAR–UCAR, accessed 2 June 2016, https://doi.org/10.5065/D61C1TXF.

Schiller, A., and J. S. Godfrey, 2003: Indian Ocean intraseasonal variability in an ocean general circulation model. *J. Climate*, **16**, 21–39, https://doi.org/10.1175/1520-0442(2003)016<0021:IOIVIA>2.0.CO;2.

Sengupta, D., and M. Ravichandan, 2001: Oscillations of the Bay of Bengal sea surface temperature during the 1998 summer monsoon. *Geophys. Res. Lett.*, **28**, 2033–2036, https://doi.org/10.1029/2000GL012548.

Sikka, D. R., and S. Gadgil, 1980: On the maximum cloud zone and the ITCZ over Indian, longitudes during the southwest monsoon. *Mon. Wea. Rev.*, **108**, 1840–1853, https://doi.org/10.1175/1520-0493(1980)108<1840:OTMCZA>2.0.CO;2.

Suhas, E., J. M. Neena, and B. N. Goswami, 2013: An Indian monsoon intraseasonal oscillations (MISO) index for real time monitoring and forecast verification. *Climate Dyn.*, **40**, 2605–2616, https://doi.org/10.1007/s00382-012-1462-5.

Vecchi, G. A., and D. E. Harrison, 2002: Monsoon breaks and subseasonal sea surface temperature variability in the Bay of Bengal. *J. Climate*, **15**, 1485–1493, https://doi.org/10.1175/1520-0442(2002)015<1485:MBASSS>2.0.CO;2.

Vialard, J., A. Jayakumar, C. Gnanaseelan, M. Lengaigne, D. Sengupta, and B. N. Goswami, 2012: Processes of 30–90 days sea surface temperature variability in the northern Indian Ocean during boreal summer. *Climate Dyn.*, **38**, 1901–1916, https://doi.org/10.1007/s00382-011-1015-3.

Vinayachandran, P. N., V. S. N. Murty, and V. R. Babu, 2002: Observations of barrier layer formation in the Bay of Bengal during summer monsoon. *J. Geophys. Res.*, **107**, 8018, https://doi.org/10.1029/2001JC000831.

——, and Coauthors, 2018: BoBBLE (Bay of Bengal Boundary Layer Experiment): Ocean–atmosphere interaction and its impact on the South Asian monsoon. *Bull. Amer. Meteor. Soc.*, https://doi.org/10.1175/BAMS-D-16-0230.1, in press.

Waliser, D. E., 2006: Intraseasonal variability. *The Asian Monsoon*, B. Wang, Ed., Springer, 203–257.

Wallcraft, A. J., A. B. Kara, C. N. Barron, E. J. Metzger, R. L. Pauley, and M. A. Bourassa, 2009: Comparisons of monthly mean 10 m wind speeds from satellites and NWP products over the global ocean. *J. Geophys. Res.*, **114**, D16109, https://doi.org/10.1029/2008JD011696.

Wang, B., P. J. Webster, and H. Teng, 2005: Antecedents and self-induction of active-break south Asian monsoon unraveled by satellites. *Geophys. Res. Lett.*, **32**, L04704, https://doi.org/10.1029/2004GL020996.

Wang, W., P. Xie, S.-H. Yoo, Y. Xue, A. Kumar, and X. Wu, 2011: An assessment of the surface climate in the NCEP climate forecast system reanalysis. *Climate Dyn.*, **37**, 1601–1620, https://doi.org/10.1007/s00382-010-0935-7.

Webster, P. J., V. O. Magaña, T. N. Palmer, J. Shukla, R. A. Tomas, M. Yanai, and T. Yasunari, 1998: Monsoons: Processes, predictability, and the prospects for prediction. *J. Geophys. Res.*, **103**, 14 451–14 510, https://doi.org/10.1029/97JC02719.

Weller, R. A., and Coauthors, 2016: Air-sea interaction in the Bay of Bengal. *Oceanography*, **29** (2), 28–37, https://doi.org/10.5670/oceanog.2016.36.

Wheeler, M. C., and H. H. Hendon, 2004: An all-season real-time multivariate MJO index: Development of an index for monitoring and prediction. *Mon. Wea. Rev.*, **132**, 1917–1932, https://doi.org/10.1175/1520-0493(2004)132<1917:AARMMI>2.0.CO;2.

Xue, Y., B. Huang, Z.-Z. Hu, A. Kumar, C. Wen, D. Behringer, and S. Nadiga, 2011: An assessment of oceanic variability in the NCEP climate forecast system reanalysis. *Climate Dyn.*, **37**, 2511–2539, https://doi.org/10.1007/s00382-010-0954-4.

Yang, B., X. Fu, and B. Wang, 2008: Atmosphere-ocean conditions jointly guide convection of the boreal summer intraseasonal oscillation: Satellite observations. *J. Geophys. Res.*, **113**, D11105, https://doi.org/10.1029/2007JD009276.

Yu, L., X. Jin, and R. A. Weller, 2007: Annual, seasonal, and interannual variability of air–sea heat fluxes in the Indian Ocean. *J. Climate*, **20**, 3190–3209, https://doi.org/10.1175/JCLI4163.1.

Zhang, Y., W. B. Rossow, A. A. Lacis, V. Oinas, and M. I. Mishchenko, 2004: Calculation of radiative fluxes from the surface to top of atmosphere based on ISCCP and other global data sets: Refinements of the radiative transfer model and the input data. *J. Geophys. Res.*, **109**, D19105, https://doi.org/10.1029/2003JD004457.